

## INTEGRAL FIELD SPECTROSCOPY OF THE CENTRAL REGIONS OF 3C 120: EVIDENCE OF A PAST MERGING EVENT

B. GARCÍA-LORENZO,<sup>1</sup> S. F. SÁNCHEZ,<sup>2</sup> E. MEDIAVILLA,<sup>1</sup> J. I. GONZÁLEZ-SERRANO,<sup>3,4</sup> AND L. CHRISTENSEN<sup>2</sup>

Received 2004 September 7; accepted 2004 November 10

### ABSTRACT

Optical integral field spectroscopy (IFS), combined with *Hubble Space Telescope* (*HST*) WFPC imaging, was used to characterize the central regions of the Seyfert 1 radio galaxy 3C 120. We carried out the analysis of the data, deriving intensity maps of different emission lines and the continua at different wavelengths from the observed spectra. Applying a two-dimensional modeling to the *HST* images, we decoupled the nucleus and the host galaxy and analyzed the host morphology. The host is a highly distorted bulge-dominated galaxy, rich in substructures. We developed a new technique to model the IFS data extending the two-dimensional modeling (hereafter three-dimensional modeling). Using this technique, we separated the Seyfert nucleus and the host galaxy spectra and derived a residual data cube with spectral and spatial information of the different structures in 3C 120. Three continuum-dominated structures (named A, B, and C) and three other extended emission-line regions (EELRs, named E<sub>1</sub>, E<sub>2</sub>, and E<sub>3</sub>) are found in 3C 120, which does not follow the general behavior of a bulge-dominated galaxy. We also found shells in the central kiloparsec that may be remnants of a past merging event in this galaxy. The origin of E<sub>1</sub> is most probably due to the interaction of the radio jet of 3C 120 with the intergalactic medium (Axon et al. 1989; Sánchez et al. 2004a). Structures A, B, and the shell at the southeast of the nucleus seem to correspond to a larger morphological clumpy structure that may be a tidal tail, a consequence of the past merging event. We found a bright EELR (E<sub>2</sub>) in the innermost part of this tidal tail, nearby the nucleus, which shows a high ionization level. The kinematics of the E<sub>2</sub> region and its connection to the tidal tail suggest that the tail has channeled gas from the outer regions to the center.

*Subject headings:* galaxies: individual (3C 120) — galaxies: ISM — galaxies: kinematics and dynamics — galaxies: Seyfert

*Online material:* color figures

### 1. INTRODUCTION

Radio galaxies are excellent laboratories to disentangle the role of central active nuclei in the evolution of host galaxies and the relation between intergalactic environment and the central activity. The complex structure of radio galaxies makes it difficult to carry out specific optical studies in this matter. Fortunately, the recent technical and computational improvements on integral field spectroscopy (IFS) open new frontiers to a multitude of astronomical projects. In the particular case of radio galaxies, IFS data allow us to separate the different components and to perform an independent analysis of the various subsystems and their evolution.

Object 3C 120 is a Seyfert 1 galaxy at a redshift of  $z = 0.033$ . It has been studied extensively at many wide-range wavelengths, with special attention in X-ray and radio frequencies (e.g., Walker et al. 1987; Moles et al. 1988; Walker 1997; Ogle et al. 2005). Although 3C 120 was classified as an early-type galaxy based on a visual inspection of ground-based images (Zwicky & Zwicky 1971), Sargent (1967) reported a faint spiral structure. However, its optical morphology is still not clear, showing an elliptical shape with some peculiarities (Hansen et al. 1987), and

could be a merger remnant galaxy (Moles et al. 1988). Spectroscopic analysis has shown that 3C 120 presents a rotation curve most likely indicating the presence of an undetected disk (Moles et al. 1988). Based on this result, 3C 120 is normally quoted as an early-type spiral or S0 galaxy (Moles et al. 1988).

Although Seyfert galaxies are generally considered to be radio-quiet objects, 3C 120 is an active radio-loud source showing a superluminal one-sided jet that extends  $\sim 25''$  out of the core (Readhead et al. 1979; Walker et al. 1988; Walker 1997). Different authors (e.g., Baldwin et al. 1980; Pérez-Fourmon et al. 1986; Soubeyran et al. 1989; Hua 1988) reported the existence of several continuum-dominated and emission-line-dominated structures in this object. Some of these structures have a clear relation with the radio jet. Hjorth et al. (1995) detected a continuum-dominated optical counterpart of the radio jet using deep broadband ground-based images. On the other hand, an EELR (E<sub>1</sub>) associated with the jet was found  $\sim 5''$  west of the nucleus (Hua 1988; Axon et al. 1989; Sánchez et al. 2004a). The nature of the remaining structures is still unclear (e.g., Pérez-Fourmon et al. 1986; Moles et al. 1988).

This paper compiles data from IFS optical observations of 3C 120 using the optical fiber system INTEGRAL covering a central region of  $\sim 16'' \times 12''$  field of view. We combined our IFS data with high-resolution *Hubble Space Telescope* (*HST*) images. We describe the optical fiber instrument, observations, and data reduction in § 2. In § 3 we describe the emission-line profiles in the circumnuclear region of 3C 120 and present two-dimensional spectral diagrams for different emission lines (Appendix A). In the following sections we present the stellar morphology and the structures detected (§ 4.1), the average colors of the galaxy and

<sup>1</sup> Instituto de Astrofísica de Canarias, 38205 La Laguna, Tenerife, 38200 Canary Islands, Spain; bgarcia@l1.iac.es.

<sup>2</sup> Astrophysikalisches Institut Potsdam, An der Sternwarte 16, 14482 Potsdam, Germany.

<sup>3</sup> Instituto de Física de Cantabria, UC-CSIC, Av. de Los Castros S/N, 35005 Santander, Spain.

<sup>4</sup> Department de Física Moderna, Facultat de Ciències, UC, Av. de Los Castros S/N, 35005 Santander, Spain.

the colors of those structures (§ 4.2), and the emission-line morphology and ionization structure (§ 4.3). In § 5 we apply a new technique to separate the spectra of different components co-existing in 3C 120 and analyze the properties of each component. We present the velocity field of the central region of 3C 120 and the discussion of several kinematic perturbations in § 6. A distance of 198 Mpc is assumed for 3C 120 throughout the paper ( $H_0 = 50 \text{ km s}^{-1} \text{ Mpc}^{-1}$ ), which corresponds to a scale of  $\sim 1 \text{ kpc arcsec}^{-1}$ .

## 2. EXPERIMENTAL SETUP, OBSERVATIONS, AND DATA REDUCTIONS

### 2.1. Integral Field Spectroscopy

IFS optical observations with fibers are based on the idea of connecting the focal plane of the telescope with the spectrograph slit using a fiber bundle. In this way, when an extended object is observed, each fiber receives light coming from a particular region of the object. Each individual spectrum appears well separated on the detector; therefore, spatial information and spectral information are collected simultaneously. The wavelength limitations essentially depend on the characteristics of the spectrograph itself. The spatial resolution depends on the fiber sizes and the prevailing seeing conditions during the observations. The spatial coverage of fiber systems is relatively small (for a counterexample see LeFevre et al. 2003), but they are very useful when studying small-size objects, such as the circumnuclear region of nearby active galaxies (e.g., García-Lorenzo et al. 2001), blue compact dwarf galaxies (e.g., Cairós et al. 2002), or gravitational lenses (e.g., Motta et al. 2002; Wisotzki et al. 2003).

IFS of 3C 120 was obtained on 2003 February 26 at the Observatorio del Roque de los Muchachos (ORM) on the island of La Palma, Spain. The 4.2 m William Herschel Telescope (WHT) was used in combination with the fiber system INTEGRAL (Arribas et al. 1998, 1999; Mediavilla et al. 1998) and WYFFOS (Bingham et al. 1994). The observations were carried out under photometric conditions and an average seeing of  $1''.2$ . The standard bundle 2 of INTEGRAL was used during these observations. This bundle consists of 219 fibers, each one with a diameter of  $0''.9$  projected on the sky. A central rectangle is formed by 189 fibers covering a field of view of  $16'' \times 12''.3$ , and the remaining 30 fibers form a ring with a diameter of  $90''$ . Figure 1 illustrates the actual distribution of the science fibers on the focal plane.

WYFFOS was equipped with a  $300 \text{ groove mm}^{-1}$  grating centered on  $5500 \text{ \AA}$  (spectral coverage:  $3500\text{--}9000 \text{ \AA}$ ). A Tek6 CCD array of  $1124 \times 1124$  pixels of  $24 \text{ \mu m}$  size was used, giving a linear dispersion of about  $3 \text{ \AA pixel}^{-1}$ . With this configuration, and pointing to the central region of 3C 120, three exposures of 1800 s each were taken. The data were reduced using IRAF standard routines (Tody 1986). Although the reduction of IFS data from fiber-based instruments does not differ significantly from standard spectroscopic data reduction, we describe briefly in this section the reduction procedure.

A master bias frame was built by averaging different bias frames taken during the night. This bias frame was then subtracted from the science frames. In observations with optical fibers, flat fields are obtained by illuminating the focal plane uniformly and obtaining spectra (the so-called flat spectra). Thus, for a particular wavelength, the differences in response among fibers dominate the flat-spectra shape. These differences are due to their distinct focal ratio degradation, position at the entrance of the spectrograph, etc. In this way, flat spectra are used to homogenize the response of all the fibers. Flat spectra are also

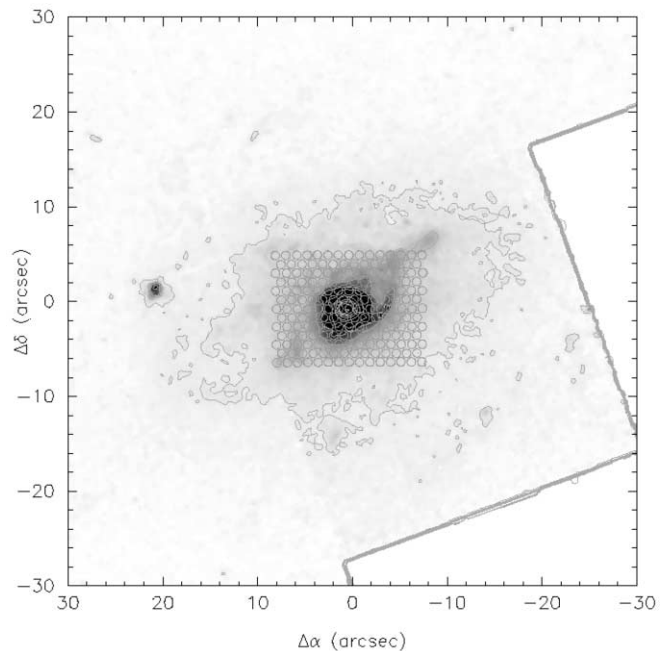


FIG. 1.—F555W-band image of 3C 120 taken with the *HST* WFPC. The spatial distribution of the science fibers at the focal plane of the 4.2 m WHT has been overlaid. North and east are up and left, respectively, as usual. The orientation is the same in all figures in this paper. [See the electronic edition of the *Journal* for a color version of this figure.]

used to obtain the polynomial fits to define the fiber path along the detector and extract the individual spectra from the whole image. Each spectrum appears well separated on the detector, with a width of approximately 2 pixels in the spatial direction (according to the core fiber image size of the fiber bundle used for these observations). The trace and extraction of individual spectra were performed using the standard routine APALL of IRAF. After this operation, frames of  $1124 \times 1124$  pixels were reduced to  $1040 \times 219$  pixels: each pixel in the spatial direction contains the spectrum of each particular fiber, with a total of 219 fibers.

The wavelength calibration was done using the IDENTIFY and REIDENTIFY routines of IRAF. In order to carry out this procedure, we selected several isolated and well-distributed arc lines. Although it might be difficult to determine the actual uncertainty produced by the wavelength calibration, we have used the skylines in our spectra to estimate the final wavelength errors, being smaller than  $35.5$  and  $29.5 \text{ km s}^{-1}$  at blue and red wavelengths, respectively.

The SP 1045+378 flux standard star (Isaac Newton Group Database) was observed the same night and under similar conditions as for 3C 120. The standard star has been used to calibrate a flux ratio by comparing with the standard-star flux tables of Stone (1977). We reduced the SP 1045+378 frames in a similar way as with the object frames, correcting them for differential atmospheric refraction (Filippenko 1982) using E3D (Sánchez 2004). Then, we extracted the observed spectrum of the star by co-adding the spectra of the central 37 fibers, which includes  $>99\%$  of the total flux. Comparing this observed spectrum with the flux-calibrated spectrum of SP 1045+378, we derived a sensitivity curve that we used to calibrate the object frames.

We combine the IDA tool (García-Lorenzo et al. 2002) and the Euro3D visualization package (Sánchez 2004) to analyze the data and generate two-dimensional maps of any spectral feature (intensity, velocity, width, etc.). Maps recovered from spectra are

TABLE 1  
SUMMARY OF PROPERTIES OF THE *HST* IMAGES

Band	Exposure Time (s)	$3\sigma$ Limiting Magnitude (mag arcsec <sup>-2</sup> )	Magnitude	Magnitude NED
F555W ( <i>V</i> ) .....	2040	25.3	14.94	14.7
F547M ( <i>V'</i> ) .....	2300	25.1	14.35	...
F675W ( <i>R</i> ) .....	2250	25.3	13.74	13.9
F814W ( <i>I</i> ) .....	2236	24.9	<sup>a</sup>	12.9

<sup>a</sup> Peak saturated.

images of  $51 \times 37$  pixels with a scale  $0''.3 \text{ pixel}^{-1}$ . While the spatial sampling of the used INTEGRAL configuration is  $0''.9$  (that is, the fiber diameter of the bundle 2), the centroid of any peak in our maps can be measured with an accuracy of around  $\frac{1}{5}$  of the fiber diameter, that is,  $\sim 0''.2$  (e.g., Mediavilla et al. 1998).

## 2.2. *HST* Imaging

Wide-Field Planetary Camera (WFPC) images of 3C 120 in different bands are available on the archive of *HST*. We obtained these images to study the morphology of this object. Table 1 summarizes the properties of these images. The data set comprises three broadband images (F555W, F675W, and F814W), which roughly corresponds to the standard *V*, *R*, and *I* bands, and a medium-band image (F547M). These images basically sample the continuum emission in 3C 120, since the equivalent width of mostly all of the emission lines is very small compared to the width of the bands. However, there is a nonnegligible contamination, dominated by the [O III] and H $\beta$  emission lines in the F555W-band image (and H $\alpha$  in the F675W-band image). The F547M-band image can be used as an estimation of the pure continuum emission, since the emission lines are at the edge of its transmission curve. The data set is deep enough to study the different structures present in this object (Soubeyran et al. 1989).

## 3. ATLAS OF SPECTRA

Figure 2 shows the nuclear spectrum of 3C 120 in the full wavelength range. This spectrum has been obtained by co-adding the seven spectra closest to the continuum peak. This is almost equivalent to a hexagonal aperture of  $1''.6$  in radius centered at the optical nucleus of 3C 120. We can easily recognize several emission lines and the characteristic broad component of permitted emission lines of Seyfert 1 galaxies.

In Appendix A we present the individual spectra corresponding to each of the different observed positions (fibers) in selected spectral intervals that include the most important emission lines (spectral diagrams).

### 3.1. Emission-Line Profiles

The profiles of the emission lines in the nuclear spectrum of 3C 120 show a considerable blending due to the wings of the broad component of permitted lines (Fig. 2). The H $\delta$  profile appears to be considerably broader than any other Balmer line, but this is not the case of H $\delta$  as previously found by other studies (Phillips & Osterbrock 1975; Baldwin et al. 1980). The He I  $\lambda 5876$  shows also a considerable broadening. At this step, we cannot discuss the origin of these features in terms of recombination models and reddening effects because the nuclear spectrum in Figure 2 includes the contribution of the nucleus and the surrounding galaxy. In § 5 we separate both contribu-

tions and will be in a position to tackle this discussion. The low spectral resolution of the current IFS data prevents the detection of double peaks reported by Axon et al. (1989). However, the emission lines show asymmetric profiles in some locations outside the central region.

## 4. DATA ANALYSIS AND RESULTS

### 4.1. Broadband Distribution and Morphological Structures

Broadband images of 3C 120 were recovered from our IFS data by co-adding the flux in spectral ranges that mimic the bandpasses of the previously refereed *HST* images and using an interpolation routine (Sánchez 2004; García-Lorenzo et al. 2002). The specific wavelength ranges for each band were 3900–4900 Å (*B* band), 5000–6000 Å (*V* band), 5600–5700 Å (*V'* band), 6100–7100 Å (*R* band), and 7550–8550 Å (*I* band). All images show a bright nucleus on top of a weak host galaxy. Figure 3a presents the intensity map corresponding to the *V*-band filter. The intensity contours have an elliptical shape, except for those at around  $4''$  from the central peak, showing an elongation toward the west. There are remarkable similarities between the restored map (Fig. 3a) and the F555W-band image from *HST* (Fig. 3b), despite the differences in wavelength ranges and spatial sampling. The superior resolution of the *HST* images

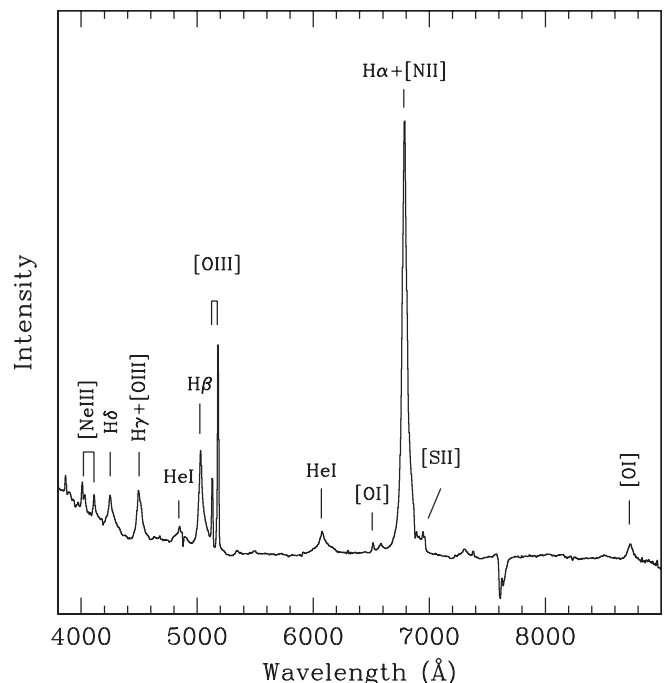


FIG. 2.—Nuclear spectrum in the full spectral range. This spectrum corresponds to a hexagonal aperture of  $1''.6$  in radius centered on the optical nucleus.

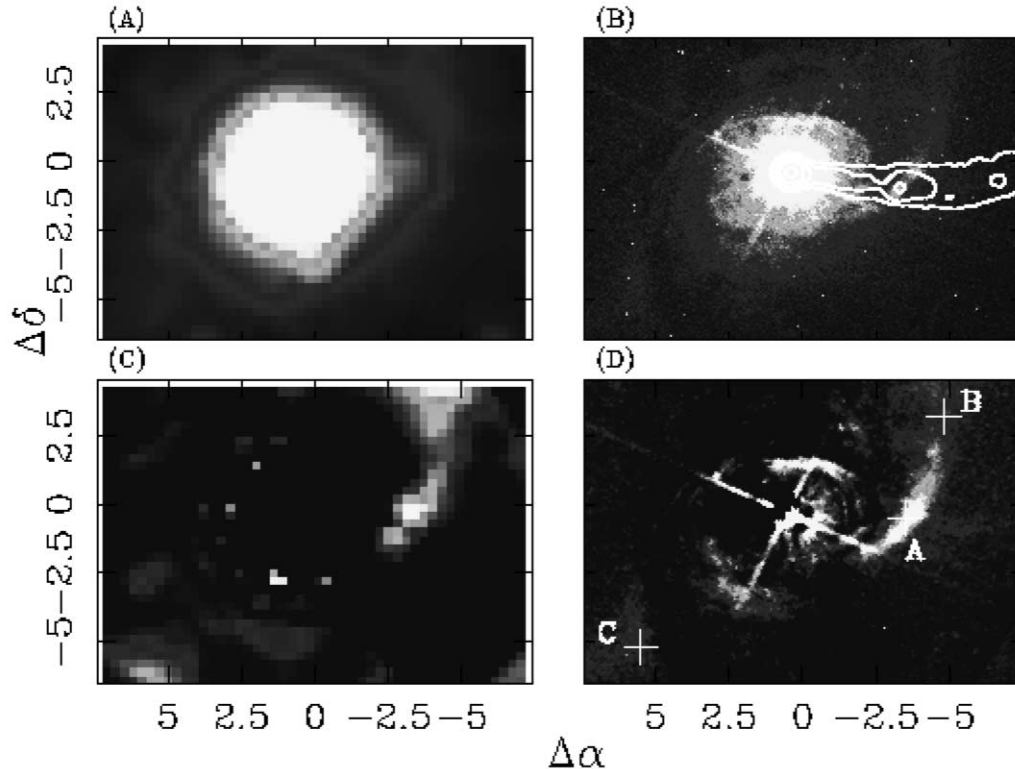


FIG. 3.—(a) Two-dimensional distribution of the continuum emission of 3C 120 derived from the IFS data by integrating the signal in the spectral range 5100–6100 Å, similar to that range covered by the *V*-band filter. (b) F555W-band image of the same central region of 3C 120 obtained with the *HST* PC ( $0''.046 \text{ pixel}^{-1}$ ). Different continuum-dominated structures already detected from ground-based observations are labeled using the nomenclature from Soubeyran et al. (1989). The contour plot shows the radio map at 4885 MHz (Walker 1997). (c) *V*-band residual image after subtraction of the galaxy template derived by a two-dimensional modeling from the *V*-band image shown in (a). (d) F555W-band residual image derived by subtracting a galaxy template obtained by a two-dimensional modeling from the F555W-band image shown in (b). [See the electronic edition of the *Journal* for a color version of this figure.]

allows us to directly detect several structures. These structures have been previously reported subtracting a galaxy template to broadband and narrowband ground-based images (e.g., Baldwin et al. 1980; Pérez-Fournon et al. 1986; Hua 1988; Soubeyran et al. 1989). We have labeled, using the nomenclature introduced by Soubeyran et al. (1989), the different detected structures (Fig. 3b). The *HST* F555W-band image allows us to resolve them, showing a richer level of structures. In particular, structures B and C are composed of a smoothed low surface brightness component and more luminous clumpy substructures. Structure A seems to be more collimated, as previously noticed by ground-based imaging, which explains why it was initially confused with the optical counterpart of the radio jet (e.g., Pérez-Fournon et al. 1986). It shows also a low surface brightness component and four clear clumps. We overplot in Figure 3b the radio map at 4885 MHz (Walker 1997), showing that structure A is most likely related to structure B rather than to the radio jet. Indeed, the *HST* images suggest that both structures belong to a sequence of clumpy knots that are physically connected. Dust lines and shell structures not detected from the ground are seen in the inner regions. Two shell arcs at  $\sim 1''$  north and south of the central peak are clearly detected in the *HST* images. Although previous *HST* images show extensions to the northwest and southeast in the inner region of 3C 120 (Zirbel & Baum 1998), to our knowledge this is the first time that the shell structure is clearly visible. The north and south shells are hereafter named  $S_N$  and  $S_S$ , respectively. The  $S_S$  seems to be connected to structure A by a faint tail.

A two-dimensional modeling of the broadband images was performed using GALFIT (Peng et al. 2002) to obtain a clear

picture of the morphology of 3C 120. This program has been extensively tested in the image decomposition of QSOs/hosts (Sánchez et al. 2004b). The two-dimensional model comprises a narrow Gaussian function (to model the nucleus) and a galaxy template (to model the galaxy), both convolved with a point-spread function (PSF). We performed the fit twice, first using a Sersic law (Sersic 1968) to characterize the galaxy and then using a de Vaucouleurs law (de Vaucouleurs 1948). This method allows us to determine the morphological type of the host galaxy, based on the obtained Sersic index, and to get a good determination of the galaxy flux, based on modeling the de Vaucouleurs law (Sánchez et al. 2004b). The PSF was created using a field star for the analysis of the *HST* images and a calibration star for the analysis of the broadband images recovered from the IFS data.

We applied first the fitting technique to the *HST* images because of their better spatial resolution. The nucleus was saturated in the *HST* F814W band, which prevents us from performing a two-model fitting and limits the reliability of any morphological classification, which strongly depends on the shape of the profile in the inner regions. To derive a rough estimation of the host magnitude, we masked the nucleus and fixed the scale to the average of the values derived in the other available *HST* bands. Further checks, explained below, demonstrated that this approach was valid. Table 2 summarizes the results from this analysis. For each band it shows the derived Sersic index, the nucleus and host magnitudes, and the effective radius of the host galaxy. The derived Sersic indices, all near or larger than the nominal value of 4 for an early-type galaxy, confirm the morphological classification of the host galaxy of 3C 120 as a bulge-dominated galaxy.

TABLE 2  
SUMMARY OF THE RESULT FROM THE TWO-DIMENSIONAL MODELING

Band	$n$	$m_{\text{nuc}}$	$m_{\text{host}}$	$r_e$ (kpc)	$a/b$	P.A. (deg)
F555W.....	4.7	16.1	15.4	1.9	0.87	-16.8
F547M.....	4.5	16.9	14.5	2.9	0.86	-18.6
F675W.....	6.7	16.1	13.9	2.8	0.73	-19.1
F814W.....	...	...	13.2	...	0.94	-18.5

We subtracted the object template (galaxy+nucleus) derived by the two-dimensional modeling from the original images, obtaining a residual image for each band. These residual images were used to study the properties of the different structures, once decontaminated from the smooth component. As an example, the residual images of the  $V$  band and the *HST* F555W band are shown in Figures 3c and 3d, respectively. The already quoted structures are now clearly identified. The  $S_S$  shell coincides with an extended emission-line region (EELR) previously detected in this object (Hua 1988; Soubeyran et al. 1989; Sánchez et al. 2004a) and labeled  $E_2$  (Soubeyran et al. 1989).

#### 4.2. Colors and Gaseous Distributions in 3C 120

As already quoted, all the broadband images recovered from the IFS data show a morphology similar to that of the  $V$ -band image shown in Figure 3a. Combining these recovered broadband maps, we obtained color maps of 3C 120. Figure 4a shows the  $V - I$  color map derived from the IFS data. It shows a blue

circumnuclear region elongated to the southwest. The elongation toward the west seen in the broadband images has also a counterpart in the color maps showing bluer colors at a region  $\sim 4''.5$  west of the nucleus than its surroundings. Figure 4b presents the  $V - I$  color map derived from the F555W- and F814W-band *HST* images. Despite their different spatial resolution, Figures 4a and 4b present remarkable similarities. The different structures quoted in § 4.1 show bluer  $V - I$  colors than the average color of the host galaxy, as already noticed (e.g., Fraix-Burnet et al. 1991). Figure 4b also shows evidence for two weaker shells farther from the central peak than  $S_N$  and  $S_S$  but also at the north and south. However, these “secondary” shells are fainter, being at the detection limit.

Both the  $V$ -band and the F555W-band images are contaminated by the emission from  $[\text{O III}]$  and  $\text{H}\beta$ . A rough estimation of how strong that contamination is can be obtained by subtracting a scaled continuum image in a narrowband filter without any contamination from emission lines. Figure 4c shows the residual image of the INTEGRAL  $V$ -band image after the subtraction of an adequate continuum (the  $V'$ -band image). A similar estimation was performed for the *HST* images, subtracting the continuum-dominated F547M-band image from the F555W-band image (Fig. 4d). This image was smoothed using an  $11 \times 11$  pixel median kernel to increase the signal-to-noise ratio. The resulting maps are a rough estimation of the distribution of the  $[\text{O III}] + \text{H}\beta$  emission. The position of two of the EELRs detected in this object (hereafter  $E_1$  and  $E_2$ ) is indicated (Soubeyran et al. 1989; Sánchez et al. 2004a). The residual images of the continuum, after subtracting a model template (Figs. 3c and 3d), are overplotted for comparison purposes. The  $S_N$  and  $S_S$  shells show a

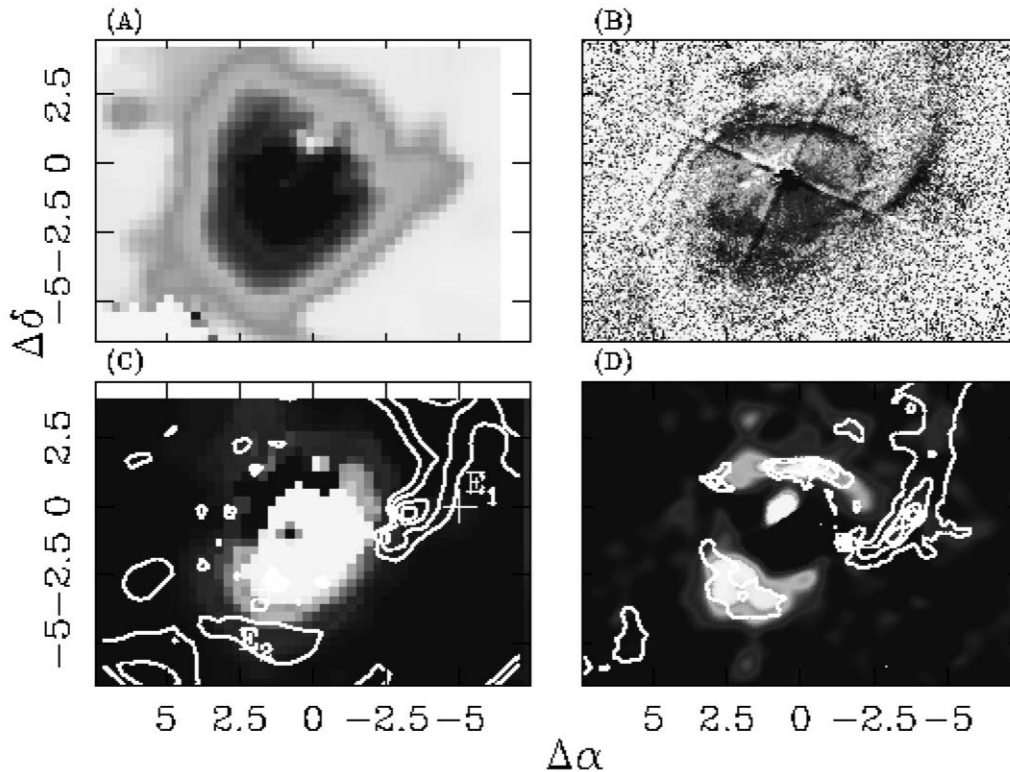


FIG. 4.— (a)  $V - I$  color image derived from the  $V$  and  $I$  maps recovered from the IFS data. (b)  $V - I$  color image obtained from the F555W- and F675W-band *HST* images. The image has been smoothed with a  $3 \times 3$  pixel median kernel. (c) Residual  $V$  map (similar to an ionized gas map) derived by subtracting a continuum recovered from the IFS data (5600–5700 Å) avoiding the contribution of any bright emission line and scaled. (d) Residual image obtained by the subtraction of the F547M-band image from the F555W-band image, once scaled by the differences of the photometric zero points. The contour plot corresponds to the F555W-band residual image shown in Fig. 3d. Labels indicate the previously detected EELRs (Soubeyran et al. 1989; Sánchez et al. 2004a). [See the electronic edition of the *Journal* for a color version of this figure.]

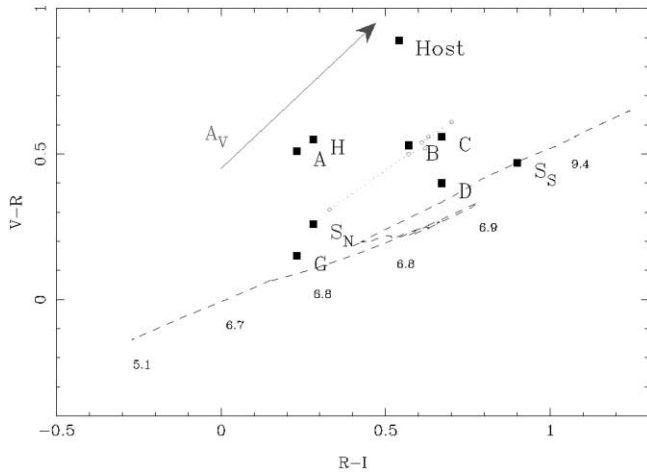


FIG. 5.— $V - R$  colors as a function of the  $R - I$  colors of the host galaxy and the different structures found in 3C 120. The dashed line shows the location of a single stellar population model at different ages (Bruzual & Charlot 2003). The values indicate the logarithm of the age in Gyr. The dotted line shows the average colors of different galaxy types (E, Sab, Sbc, Scd, and Irr), obtained from Fukugita et al. (1995). The arrow shows the effect of dust in the colors for an absorption of  $A_V \sim 1.5$  mag. Errors of the individual colors are 0.1 and 0.26 mag in  $V - R$  and  $R - I$ , respectively. [See the electronic edition of the *Journal* for a color version of this figure.]

strong gaseous emission in the *HST* images, which in the  $S_5$  extends toward the  $E_2$  region.

Figure 5 shows the  $V - R$  colors of the host galaxy and the different structures as a function of the  $R - I$  colors. As already noticed in the color image, the structures have bluer  $V - R$  colors than the host galaxy. This indicates most probably the presence of somewhat younger stellar populations associated with them. However, they show a wider range of  $R - I$  colors than that of  $V - R$  colors. Indeed, the average  $R - I$  color of the host galaxy is within the range of  $R - I$  colors of the different structures. The color-to-color distribution derived from synthetic models has been included in the figure for comparisons. The dashed line shows the colors of single stellar populations calculated using the Bruzual & Charlot (2003) models. We assumed a solar metallicity and a Chabrier (2003) initial mass function (IMF). The labels indicate the logarithm of the stellar population ages in Gyr. In general terms, the color-to-color distribution does not match with that simple model, apart from the case of the  $S_N$  and  $S_5$  shells. For the remaining structures, the  $R - I$  colors correspond on average to a young stellar population of  $\sim 6 \times 10^8$  Gyr, but the  $V - R$  colors correspond to older stellar populations. This may indicate that the real populations are a composite of populations. The dotted line shows the colors of different galaxy types (E, Sab, Sbc, Scd, and Irr; Fukugita et al. 1995), which mainly correspond to different mixes of stellar populations. The  $R - I$  color of the host galaxy mainly corresponds to an Sab–Scd galaxy. On average, the structures have  $V - R$  colors that correspond to the same kind of galaxies (Sab–Scd), but their  $R - I$  colors expand over all the ranges of possible colors.

So far we have ignored the effects of dust in the color-to-color distribution shown in Figure 5. However, the dust content in 3C 120 is rather high; an average value of  $A_V \sim 4$  mag has been estimated (Sánchez et al. 2004a). Dust extinction reddens both  $V - R$  and  $R - I$  colors in an almost similar way (Fitzpatrick 1999). The effects of dust in the color-to-color distribution are illustrated by an arrow in Figure 5. It is clear that the dust is not homogeneously distributed in the galaxy: e.g., typical dust lanes are seen in Figure 3b. A combined effect of different

stellar populations and a nonhomogeneous distribution of dust could explain the observed color-to-color distribution. In that case, the  $S_N$  and  $S_5$  structures would be dust-free areas dominated by a single stellar population.

However, results from broadband colors should be taken with care. The contamination of broadband filters by strong emission lines can drastically affect the morphology of color maps. In the case of 3C 120 the problem is even worse because of the contribution and contamination from the broad component of the Balmer emission lines in the central regions.

### 4.3. Line Intensity Maps and Ionization Structure

We performed a line profile fitting and deblending in order to study the integrated high- and low-ionization gas distribution, their physical properties, and kinematics. We fitted a single Gaussian to any of the bright emission lines in the spectra. For the Balmer lines, we included a second broader Gaussian to fit the wide line from the broad-line region (BLR). In spite of our poor spectral resolution, we found that several spectra have evidence of substructures, showing asymmetric profiles with blue or red wings indicating the presence of several gaseous systems in 3C 120. Indeed, previous authors (Axon et al. 1989) reported the existence of several components in the emission lines of 3C 120, but to apply a line profile decomposition to separate the different gaseous components would be unrealistic because of the low spectral resolution of the current IFS data. The broad component of the Balmer lines is confined to the nucleus, discarding an extended broad emission line region.

Figure 6 shows the intensity maps of  $[\text{O III}] \lambda 5007$  (Fig. 6a) and  $\text{H}\alpha$  (Fig. 6b) after deblending. Intensity contours of ionized gas are clearly elongated toward the  $E_2$  structure. Emission-line maps present an elongation to the west, forming a clear secondary peak at around  $5''$  from the nucleus in the  $[\text{O III}]$  intensity map. This secondary peak corresponds to the  $E_1$  structure previously quoted (§ 4.2). The ratio of the  $\text{H}\alpha$  intensity of the nucleus and  $E_1$  is much smaller than that of  $[\text{O III}] \lambda 5007$ , suggesting a high-ionization nature of the latter. The nuclear region shows a low-ionization degree in the  $[\text{O III}] \lambda 5007/\text{H}\beta$  map surrounded by a ring of high ionization (Fig. 6c), with larger values at the south of the nucleus, coincident with the location of  $E_2$ . A high-ionization region expands from the ring to the west, increasing the ionization degree along this direction. The  $[\text{N II}] \lambda 6584/\text{H}\alpha$  line ratio map (Fig. 6d) also shows a ring structure, surrounding the nuclear region. The  $E_1$  is on the path of the 3C 120 radio jet, as well as the continuum-dominated structure  $A$ . The high  $[\text{O III}]/\text{H}\beta$  ratio of  $E_1$  (Fig. 6c) discards a relation between  $A$  and  $E_1$ , assuming that  $A$  is a star-forming region in a spiral arm or a tidal tail, and points, more likely, to a direct connection between  $E_1$  and the radio jet (Sánchez et al. 2004b). While the nucleus and the  $A$  region present  $[\text{O III}] \lambda 5007/\text{H}\beta$  and  $[\text{N II}] \lambda 6584/\text{H}\alpha$  ratios at the limit of  $\text{H II}$  regions in a diagnostic diagram (Veilleux & Osterbrock 1987), those ratios of  $E_1$  and its west surroundings are placed on the high-ionization region.

The distribution of the  $\text{H}\alpha/\text{H}\beta$  line ratio (Fig. 6e) shows a dust lane crossing 3C 120 along the southeast-northwest direction. The high Balmer decrement at the west points to a high dust obscuration around  $E_1$ . However, we cannot rule out that the high  $\text{H}\alpha/\text{H}\beta$  ratio may be related to the low signal-to-noise ratio of the narrow component of  $\text{H}\beta$  in the circumnuclear region of the galaxy. The electronic density derived from the  $[\text{S II}] \lambda 6716/\lambda 6730$  presents a patchy structure, showing an enlargement in the location of  $E_1$ . In the next section, the ionization

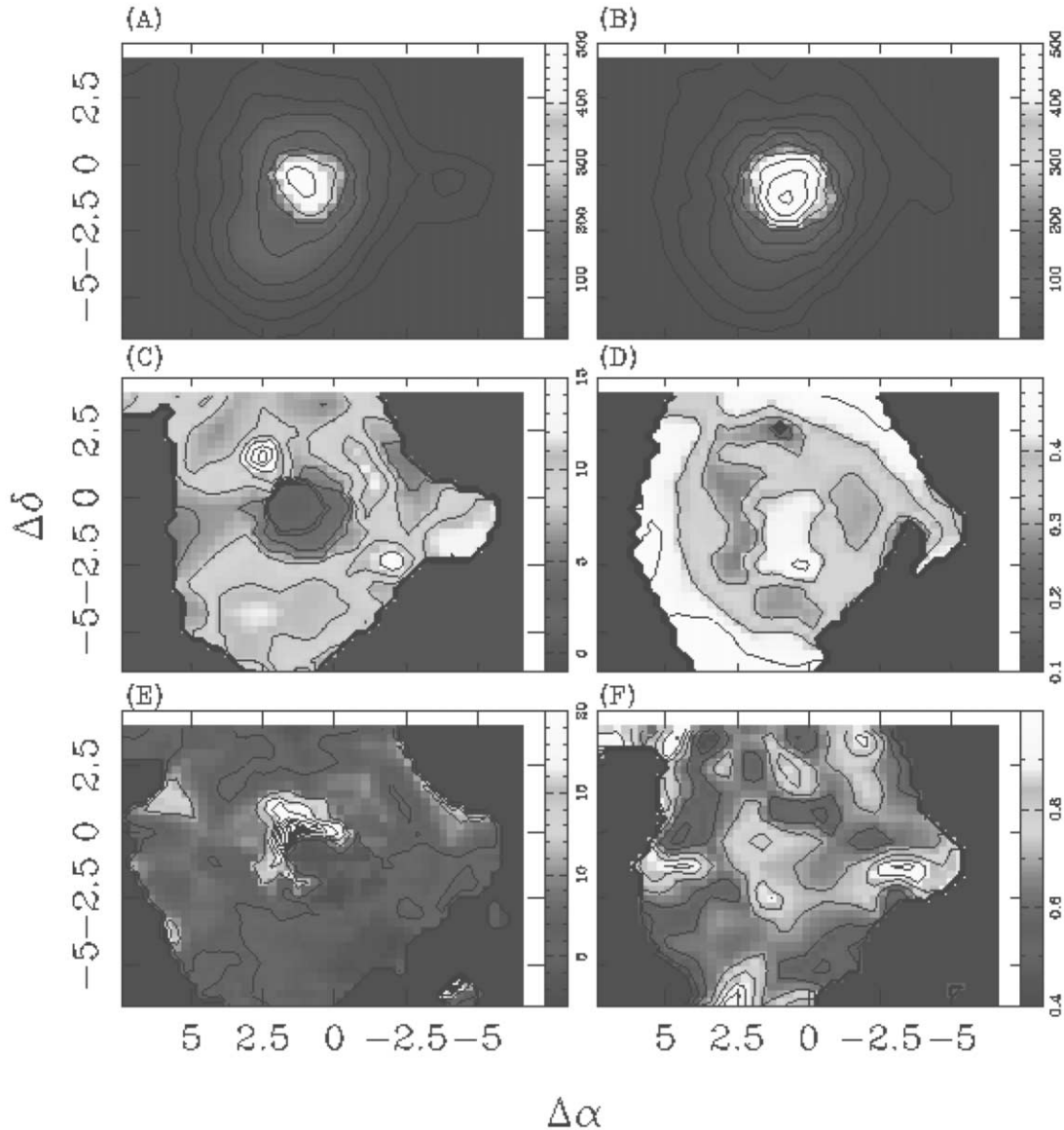


FIG. 6.—Integrated intensity maps of (a)  $[\text{O III}] \lambda 5007$  and (b)  $\text{H}\alpha$  emission lines derived by a Gaussian fitting. In the circumnuclear region, we have included a second broad Gaussian to  $\text{H}\alpha$ . Dividing line intensity maps, we derive (c) the ionization map  $[\text{O III}]/\text{H}\beta$ , (d)  $[\text{N II}]/\text{H}\alpha$  two-dimensional distribution, (e) the extinction  $\text{H}\alpha/\text{H}\beta$  map, and (f) the electronic density distribution  $[\text{S II}] \lambda 6716/[\text{S II}] \lambda 6730$ . [See the electronic edition of the *Journal* for a color version of this figure.]

conditions of the different structures in the observed region of 3C 120 are studied in detail.

### 5. DECOUPLED SPECTRA OF THE DIFFERENT COMPONENTS IN 3C 120

In the previous section we used the traditional method (Gaussian fitting) to deblend the different gaseous components. IFS optical observations record spatial and spectral information simultaneously. Taking advantage of this fact, we have developed a technique (hereafter three-dimensional modeling) to disentangle the spectra of the main components of 3C 120 (nucleus+host) and to obtain cleaned spectra of the different structures described above. This technique has been successfully applied recently (Sánchez et al. 2004a). A brief summary of the technique is described in Appendix B and will be explained in detail in a separate paper (S. F. Sánchez et al. 2005, in preparation). In summary, the technique provides us with a spectrum of each of the main components of the object plus a residual data cube that can be used to derive cleaned spectra of the different

structures in the object and/or analyze their morphological and kinematic properties. This is an extension of the two-dimensional modeling of images applied in § 4.1 to each of the monochromatic images of the data cube derived from IFS optical observations. We applied the three-dimensional modeling to the current data and derived the 3C 120 nucleus spectrum, the mean host galaxy spectrum, and a residual data cube of spectra.

#### 5.1. Morphological Structures from the Residual Data Cube of Spectra

To compare the results from the proposed technique to those of the traditional method, we show in Figure 7a the gray scale of the residual from the two-dimensional modeling of the *HST* F555W-band image obtained in § 4.1 (Fig. 3d). We overplotted the contours of a narrowband image centered on the continuum adjacent to the  $[\text{O III}]$  emission line ( $5204\text{--}5246 \text{ \AA}$ ) extracted from the residual data cube of spectra obtained after the three-dimensional modeling. The main continuum-dominated structures (A, B, and C) are detected  $\sim 1''$  from the nucleus. As expected,

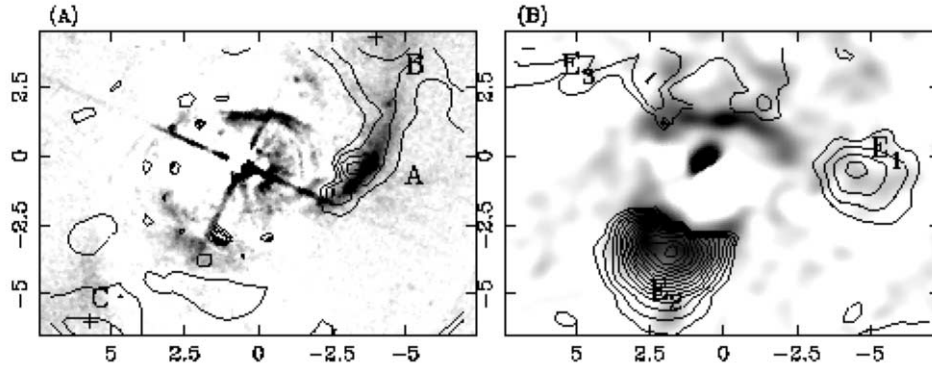


FIG. 7.— (a) Contour plot of a narrowband image centered on the continuum adjacent to the [O III] emission line (5204–5246 Å) extracted from the residual data cube, together with a gray scale of the residual from the two-dimensional modeling of the F555W-band image (Fig. 3d). (b) Contour plot of a narrowband image centered on the [O III]  $\lambda$ 5007 emission line (5170–5200 Å) extracted from the residual data cube, together with a gray scale of the F555W – F547M image shown in Fig. 3d. The different continuum-dominated (left) and emission-line-dominated (right) substructures are labeled with their corresponding names.

the shell structure detected at  $\sim 1''$  north and south of the nucleus in the *HST* images is not detected with the IFS data. A combination of the superior resolution of the *HST* images, the effects of the seeing, and the sampling of our IFS data can explain it. In Figure 7b we present the gray scale of the F555W – F547M image (obtained in § 4.2; Fig. 4d) and the contours of a narrowband image centered on the [O III]  $\lambda$ 5007 emission line (5170–5200 Å) extracted from the residual data cube. As we quoted above (§ 4.2), the F555W – F547M image is a rough estimation of the [O III]–H $\beta$  emission map. Although both images are in good agreement, IFS data are more adequate to detect EELRs that are diluted in broadband filter images, like the F555W-band one. It is possible to identify the E<sub>1</sub> and E<sub>2</sub> structures and a third region (hereafter E<sub>3</sub>) northwest of the F555W – F547M image. Soubeyran et al. (1989) already detected these emission-line regions, using narrowband imaging centered on the [O III] emission line spectral region. E<sub>1</sub> and E<sub>2</sub> are completely coincident with their reported positions. The peak of E<sub>3</sub> found by Soubeyran et al. (1989) is not included within the field of view of INTEGRAL. We are confident of our detection, and most probably we are seeing a tail previously not detected of E<sub>3</sub> toward the nucleus.

### 5.2. Spectra of the Nucleus and the Host Galaxy

Figures 8 and 9 show the spectra of the different deblended components of 3C 120. Figure 8a shows the spectrum of the nucleus. Its continuum follows roughly a power law with a slope

of  $\alpha \sim -0.5$  ( $F_\lambda \propto \lambda^\alpha$ ). It contains broad emission lines, without any trace of them in the spectrum of the host galaxy (Fig. 8b), which indicates that the decoupling technique has worked properly. The intensities of the narrow emission lines are weaker in the nucleus than in the host galaxy spectrum. Indeed, many emission lines are clearly detected in the host galaxy spectrum but not in the nucleus.

To derive the properties of the emission lines in the spectrum of the nucleus, we fitted Gaussian functions to the different emission lines. The adjacent continuum was modeled with a low-degree polynomial function. To increase the accuracy of our model, different nearby emission lines were fitted together, defining line systems with the same systemic velocity and FWHM. After several attempts, the best (and simplest) modeling was obtained including two decoupled broad systems, with  $\sim 8796$  and  $\sim 2188$  km s<sup>-1</sup>, and a narrow system, with  $\sim 700$  km s<sup>-1</sup>. Recently, Ogle et al. (2005) also reported two broad components and one narrow component for the Balmer hydrogen lines in the nucleus of this galaxy with similar velocity dispersions as those derived here. Table 3 lists the result from the fit, including the wavelength, the flux, and their 1  $\sigma$  errors for each detected line. The uncertainties in the determination of the flux of the narrow emission lines affected by line blending are high as expected. The H $\alpha$ /H $\beta$  line ratios are in the range of  $\sim 3.0$ – $3.6$  for the different line systems, in agreement with the nominal values for case B recombination (Osterbrock 1989). Therefore, both the

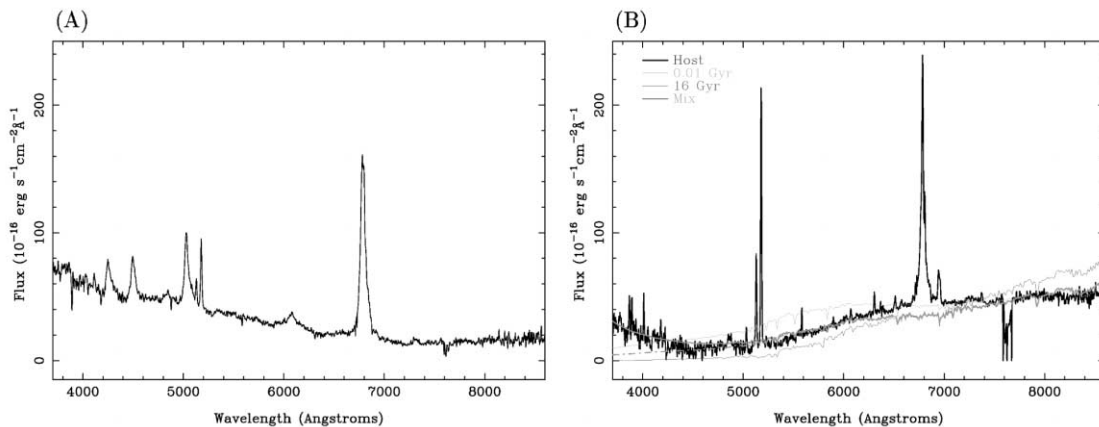


FIG. 8.— (a) Spectrum of the nucleus of 3C 120, once decontaminated from the contribution of the host galaxy. (b) Spectrum of the host galaxy together with the spectrum of synthetic models for single stellar populations of 16 Gyr, 0.01 Gyr, and a mix of both, adding (solid line) and not adding (dashed line) a power-law continuum to simulate scattered light from the nucleus. [See the electronic edition of the Journal for a color version of this figure.]

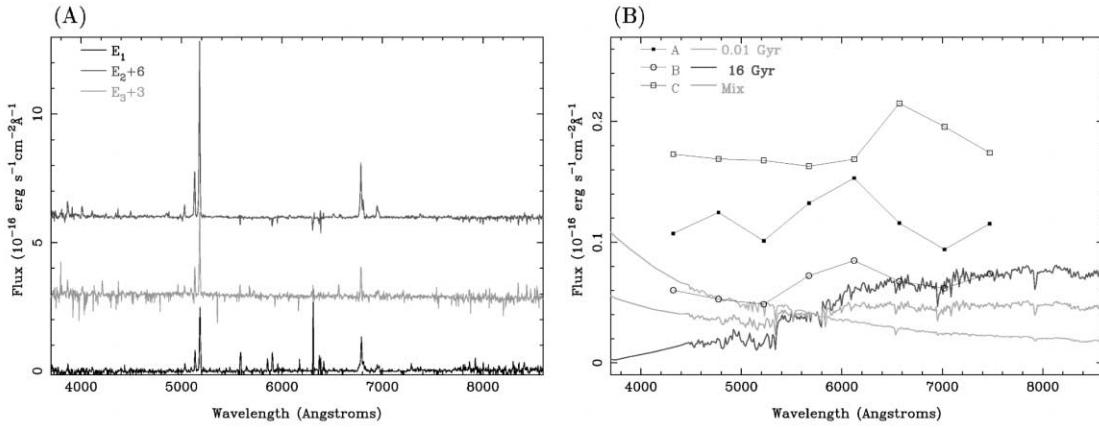


Fig. 9.—(a) Spectra of the different EELRs detected in the residual data cube. (b) Spectra of the different continuum-dominated structures detected in the residual data cube (symbols) and a median filtered version of these data (solid lines, filled squares), with a 300 Å width. [See the electronic edition of the *Journal* for a color version of this figure.]

narrow and broad emission line regions are not significantly affected by dust, as expected for a type 1 active galactic nucleus (AGN). We estimated an effective temperature of  $\sim 2.3 \times 10^5$  K using the  $([\text{O III}] \lambda 5007 + [\text{O III}] \lambda 4959)/[\text{O III}] \lambda 4363$  line ratio and the relation between this ratio and temperature (Osterbrock 1989) typical of this kind of AGN.

Figure 8b shows the average spectrum of the host galaxy together with the spectra of different synthetic models consisting of single stellar populations of different ages. We used the Bruzual & Charlot (2003) models, assuming a solar metallicity and a Chabrier (2003) IMF. The effects of dust were included in the model using the extinction curve of Fitzpatrick (1999) for a dust absorption of  $A_V \sim 4$  mag (the average value in the host galaxy, as shown below). Two extreme cases were plotted, representing an old ( $\sim 16$  Gyr) and a young stellar population ( $\sim 0.01$  Gyr). These extreme cases are a clear oversimplification, but they can be used just for qualitative comparisons. A single stellar population cannot describe the observed spectrum: the optical slope between  $\lambda \sim 5000$  and  $\sim 6500$  Å matches well with that of an old stellar population. However, the slope at larger wavelengths is flatter, more similar to that of a young stellar population. We already noticed it (§ 4.2) when we analyzed the broadband colors of the host galaxy (Fig. 5). Only a mix of different stellar populations can explain the observed spectrum.

We included in Figure 8b the spectrum of a 50/50 mix of both components. Even this simple model can describe quite well the spectrum of the host galaxy for  $\lambda > 4500$  Å. At shorter wavelengths there is an increase of the flux, which does not match with the mix model (dot-dashed line). It is well known that powerful radio galaxies show a significant blue–UV excess (Lilly & Longair 1984) more likely due to scattered light from the nucleus than to young stellar populations (McCarthy et al. 1987). This scattered light can be well described by a power law. Adding a power law to the mix model, we can describe the average host galaxy spectrum for any wavelength. Therefore, three components are needed to explain qualitatively the spectrum of the host galaxy: (1) an underlying old stellar population, (2) a young stellar population, and (3) a nebular continuum, most probably scattered light from the nucleus. We did not perform a proper fitting to determine the best fractions of the different components because it would not change the qualitative statement, and, in any case, the specific fractions will depend on the assumed synthetic models for the young and old populations and we chose them arbitrarily. The contributions of each component to the total flux are  $\sim 5\%$ ,  $\sim 55\%$ , and  $\sim 40\%$  at 4500 Å

and  $\sim 35\%$ ,  $\sim 64\%$ , and  $\sim 2\%$  at 6000 Å. Similar results have been found in the study of other powerful radio galaxies (e.g., Tadhunter et al. 1996).

Table 3 lists the results derived from fitting a single Gaussian to the emission lines in the host galaxy spectrum. As we quoted above, only narrow emission lines corresponding to a dispersion velocity of  $\text{FWHM} \sim 700$   $\text{km s}^{-1}$  are detected. These emission lines are considerably stronger than the narrow emission line region in the spectrum of the nucleus, indicating the presence of an extended narrow emission line region that extends through most of the field of view. Similar results have been found in spectroscopic studies of radio-quiet type 1 AGNs (e.g., Jahnke 2002; Jahnke et al. 2004b). The  $\text{H}\alpha/\text{H}\beta$  line ratio is  $\sim 10$ , indicating a dust absorption of  $A_V \sim 4$  mag when comparing with the nominal case B recombination value (Osterbrock 1989) and using the Fitzpatrick (1999) extinction curve. On average the host galaxy contains a rather high dust content, but the dust distribution is not uniform as we can see in Figure 6e. We estimated an effective temperature of  $\sim 14,000$  K using the  $([\text{O III}] \lambda 5007 + [\text{O III}] \lambda 4959)/[\text{O III}] \lambda 4363$  line ratio and an electron density of  $n_e \sim 10$   $\text{cm}^{-3}$  using the  $[\text{S II}] \lambda 6716/\lambda 6731$  line ratio. To derive these quantities, we used the relations between these line ratios and the measured parameters (Osterbrock 1989). The line ratios  $\log([\text{O III}] \lambda 5007/\text{H}\beta) \sim 1.2$  and  $\log([\text{N II}] \lambda 6583/\text{H}\alpha) = -0.4$  indicate most probably a direct photoionization by the UV flux from the AGN, consistent with the result shown in § 4.3.

### 5.3. Spectra of the EELRs: Origin of the Ionization

The integrated individual spectra of the structures  $E_1$ ,  $E_2$ , and  $E_3$  described in § 5.1 were extracted from the residual data cube. Figure 9a presents the spectra of each EELR ( $E_1$ ,  $E_2$ ,  $E_3$ ), which are remarkably similar. They have a clear gaseous nature, without appreciable continuum emission. This result confirms that the continuum-dominated structure A is not related to  $E_1$  as we pointed out in § 4.2. A visual inspection of the relative strength of the different lines indicates that the dominant ionization source is the AGN or shocks, rather than a star formation process. This was already noted in § 4.3 and Figure 6c for  $E_1$  and  $E_2$ . Table 4 lists the result of the Gaussian modeling of the emission lines in these spectra. Different line ratios and parameters derived from them are listed in Table 5. We included the  $[\text{O III}] \lambda 5007/\text{H}\beta$ ,  $[\text{N II}] \lambda 6583/\text{H}\alpha$ , and  $[\text{S II}] \lambda 6716/[\text{S II}] \lambda 6731$  line ratios and the derived dust absorption ( $A_V$ ), electron density ( $n_e$ ), and effective temperature ( $T_{\text{eff}}$ ). Those values of the nucleus and the host galaxy spectra were also included for

TABLE 3  
 PROPERTIES OF THE EMISSION LINES DETECTED IN THE NUCLEUS AND HOST GALAXY OF 3C 120

Name	Line	$\lambda$ (Å)	$\sigma_\lambda$	Flux ( $10^{-16}$ ergs s $^{-1}$ cm $^{-2}$ )	$\sigma_{\text{flux}}$	
Nucleus .....	H $\delta^a$	4250.33	24.12	61.25	260.78	
	H $\delta$ BL1	4249.15	24.12	319.60	583.19	
	H $\delta$ BL2	4254.50	24.12	1754.62	516.10	
	H $\gamma$	4498.42	24.12	35.08	268.68	
	H $\gamma$ BL1	4497.24	24.12	885.98	539.97	
	H $\gamma$ BL2	4502.58	24.12	790.73	422.00	
	[O III] $\lambda$ 4363	4521.98	24.12	60.99	119.60	
	He II $\lambda$ 4686 BL1	4846.66	24.12	192.56	100.54	
	He II $\lambda$ 4686 BL2	4876.41	24.12	270.39	141.18	
	H $\beta$	5024.82	0.19	75.54	479.99	
	H $\beta$ BL1	5028.23	1.76	1473.31	754.88	
	H $\beta$ BL2	5058.85	53.77	1676.73	788.82	
	[O III] $\lambda$ 4959	5125.77	0.19	163.17	35.06	
	[O III] $\lambda$ 5007	5175.36	0.19	489.58	105.20	
	He I $\lambda$ 5876 BL1	6075.86	11.62	332.05	112.13	
	He I $\lambda$ 5876 BL2	6105.86	11.62	465.42	157.05	
	[O I] $\lambda$ 6300.3	6518.52	40.42	20.34	33.63	
	[O I] $\lambda$ 6363.8	6584.19	40.42	30.34	34.81	
	[N II] $\lambda$ 6548	6784.48	2.08	9.46	57.34	
	H $\alpha$	6799.71	2.08	232.62	513.60	
	H $\alpha$ BL1	6782.94	0.58	3570.51	574.07	
	H $\alpha$ BL2	6797.59	1.15	5985.15	446.94	
	[N II] $\lambda$ 6583	6821.21	2.08	28.40	172.13	
	Host .....	[O II] $\lambda$ 3727	3867.81	10.22	477.51	60.96
		[Ne III] $\lambda$ 3869	4010.57	16.32	332.54	48.24
		[Ne III] $\lambda$ 3967	4117.10	16.32	179.77	34.32
		[S II] $\lambda$ 4072	4223.39	122.12	110.88	37.32
		H $\gamma$	4494.84	389.92	54.84	28.56
		[O III] $\lambda$ 4364	4518.40	389.92	56.88	28.32
		He II $\lambda$ 4686	4851.17	143.31	101.76	33.48
		H $\beta$	5030.04	0.82	218.05	39.72
		[O III] $\lambda$ 4959	5131.00	0.82	1164.08	161.37
[O III] $\lambda$ 5007		5180.58	0.82	3495.62	484.59	
He I $\lambda$ 5876		6072.99	23.27	45.60	47.40	
[O I] $\lambda$ 6300		6514.63	194.46	122.40	60.48	
[O I] $\lambda$ 6364		6580.30	194.46	58.08	55.20	
[N II] $\lambda$ 6548		6771.69	2.31	259.45	46.92	
H $\alpha$		6786.91	2.31	2097.63	255.97	
[N II] $\lambda$ 6583		6808.41	2.31	778.37	140.77	
[S II] $\lambda$ 6716		6946.13	32.68	368.18	96.00	
[S II] $\lambda$ 6731		6961.00	32.68	248.29	89.52	
Ar III		7377.62	291.60	108.48	69.00	

<sup>a</sup> The narrow emission lines had a velocity dispersion of  $\sim 700$  km s $^{-1}$ , while the broad emission lines have two components, BL1 and BL2, with a velocity dispersion of  $\sim 2188$  and  $\sim 8706$  km s $^{-1}$ , respectively.

comparison purposes. As we already mentioned, the ionization conditions are similar in the different EELRs, being also similar to those of the nucleus and the host. Figure 10 shows the classical diagnostic diagram of the [O III]  $\lambda$ 5007/H $\beta$  line ratio as a function of [N II]  $\lambda$ 6583/H $\alpha$  for the different components of 3C 120, including the division between AGNs and star-forming regions (Veilleux & Osterbrock 1987). The major difference is found in the position of the nucleus in the diagram, which seems to lie in the location of star-forming regions. This is most probably due to the large uncertainties in the [N II]  $\lambda$ 6583/H $\alpha$  line ratio derived for the spectrum of the nucleus, largely influenced by the deblending process of the narrow and broad emission lines, as we quoted above. The derived effective temperature ( $T \sim 1.4 \times 10^4$  K) for the host galaxy spectrum does not exclude the hot stars as a possible origin for the ionization, but the high [S II]/H $\alpha$ , [N II]/H $\alpha$ , and [O III]/H $\beta$  ratios indicate that the

average ionization for the host is the AGN or/and a shock process; i.e., the observed spectra cannot be found in H II regions. The [N II]  $\lambda$ 6583/H $\alpha$  line ratio of the E<sub>3</sub> region is lower than that value for the rest of the structures. E<sub>3</sub> is the faintest detected EELR, and it was not completely covered by our field of view, according to the [O III] maps shown by Soubeyran et al. (1989). Its spectrum is noisier and with some clear defects at specific wavelengths produced by the modeling technique. A detailed inspection of the spectrum shown in Figure 9 shows that the [N II]  $\lambda$ 6583 line is distorted by one of these defects, affecting the [N II]  $\lambda$ 6583/H $\alpha$  line ratio, the error of which is clearly larger than the formal error plotted in Figure 10. Despite these caveats, it is clear that star formation processes do not dominate the ionization of the different EELRs.

The dust content in the EELRs is lower than the mean obscuration of the host. In particular, for the E<sub>2</sub> and E<sub>3</sub> regions the dust

TABLE 4  
PROPERTIES OF THE EMISSION LINES DETECTED IN THE EELRS OF 3C 120

Name	Line	$\lambda$ (Å)	$\sigma_\lambda$	Flux ( $10^{-16}$ ergs s $^{-1}$ cm $^{-2}$ )	$\sigma_{\text{flux}}$	
E <sub>1</sub> .....	[O III] $\lambda$ 3727	3868.81	8.63	1.45	0.38	
	[Ne III]	4015.92	8.63	0.13	0.02	
	[Ne III]	4117.45	8.63	0.68	0.09	
	H $\beta$	5032.50	3.74	2.11	0.17	
	[O III] $\lambda$ 4959	5133.57	3.74	9.52	1.21	
	[O III] $\lambda$ 5007	5183.20	3.74	28.55	3.64	
	[N II] $\lambda$ 6548	6775.53	8.62	1.53	0.13	
	H $\alpha$	6790.75	8.62	16.32	1.39	
	[N II] $\lambda$ 6583	6812.25	8.62	4.62	0.40	
	[S II] $\lambda$ 6716	6948.04	58.25	2.63	0.24	
	[S II] $\lambda$ 6731	6962.91	58.25	2.06	0.21	
	E <sub>2</sub> .....	[O II] $\lambda$ 3727	3864.80	10.25	7.08	0.55
		[Ne III]	4012.37	13.09	4.29	0.35
		[Ne III]	4111.74	26.17	2.53	0.20
[S II]		4217.03	82.77	0.56	0.06	
H $\delta$		4247.03	10.82	1.02	0.11	
H $\gamma$		4493.72	10.82	2.48	0.32	
He II $\lambda$ 4686		4850.62	40.48	2.20	0.17	
H $\beta$		5028.49	0.81	4.95	0.39	
[O III] $\lambda$ 4959		5129.44	0.81	25.27	3.06	
[O III] $\lambda$ 5007		5179.03	0.81	75.82	9.18	
He I $\lambda$ 5876		6077.20	50.43	0.80	0.12	
[O I] $\lambda$ 6300.3		6513.68	40.26	1.63	0.20	
[O I] $\lambda$ 6363.8		6572.96	294.61	0.24	0.04	
[N II] $\lambda$ 6548.1		6770.28	3.38	2.77	0.23	
H $\alpha$		6785.51	3.38	25.40	2.04	
[N II] $\lambda$ 6583.6		6807.01	3.38	8.33	0.68	
[S II] $\lambda$ 6716		6946.47	16.71	5.89	0.50	
[S II] $\lambda$ 6731		6961.35	16.71	2.96	0.29	
Ar III		7378.28	51.65	1.48	0.12	
E <sub>3</sub> .....	[O II] $\lambda$ 3227	3866.04	14.72	4.54	0.87	
	[Ne III] $\lambda$ 3927	4013.15	14.72	2.39	0.28	
	H $\beta$	5032.51	39.54	2.10	0.21	
	[O III] $\lambda$ 4959	5131.26	2.71	11.06	1.53	
	[O III] $\lambda$ 5007	5180.84	2.71	33.21	4.58	
	[N II] $\lambda$ 6548	6771.15	6.12	0.41	0.01	
	H $\alpha$	6786.37	6.12	12.74	1.71	
	[N II] $\lambda$ 6584	6807.87	6.12	1.23	0.04	
	[S II] $\lambda$ 6716	6946.55	22.92	13.97	1.56	
	[S II] $\lambda$ 6731	6961.42	22.92	6.70	0.75	

absorption is almost half of the average in the host galaxy. On the other hand, the electron density in those clouds is  $\sim 10$  times lower than the average. However, this density is  $\sim 10$  times higher in the E<sub>1</sub> region, i.e.,  $\sim 100$  times larger than in the other clouds. This indicates most probably a different origin of those clouds. In Sánchez et al. (2004a) we discussed in detail the

nature of the E<sub>1</sub> emission-line region. It is most probably associated with the radio jet that crosses this cloud, compressing it as a result of its lateral expansion, and splitting it into two different kinematic regions (Axon et al. 1989; Sánchez et al. 2004a). The compression is reflected in the increase of the electron density. The nature of the ionization is not clear in this

TABLE 5  
PROPERTIES OF THE GASEOUS EMISSION OF THE DIFFERENT COMPONENTS IN 3C 120

Name	[O III] $\lambda$ 5007/H $\beta$ <sup>a</sup>	[N II] $\lambda$ 6583/H $\alpha$ <sup>a</sup>	H $\alpha$ /H $\beta$	$A_V$ (mag)	[S II] $\lambda$ 6716/[S II] $\lambda$ 6731	$n_e$ (cm $^{-3}$ )	$T_{\text{eff}}$ (K)
E <sub>1</sub> .....	1.13	-0.54	7.7	3.2	1.3	$\sim 160$	...
E <sub>2</sub> .....	1.18	-0.48	5.1	1.9	2.0	$\sim 1$	...
E <sub>3</sub> .....	1.20	-1.02	6.1	2.4	2.0	$\sim 1$	...
Nucleus <sup>b</sup> .....	0.81	-0.91	3.1	...	...	...	$2.3 \times 10^5$
Host.....	1.21	-0.43	9.8	4.0	1.5	$\sim 10$	$1.4 \times 10^4$

<sup>a</sup> In logarithms.

<sup>b</sup> Narrow emission lines.

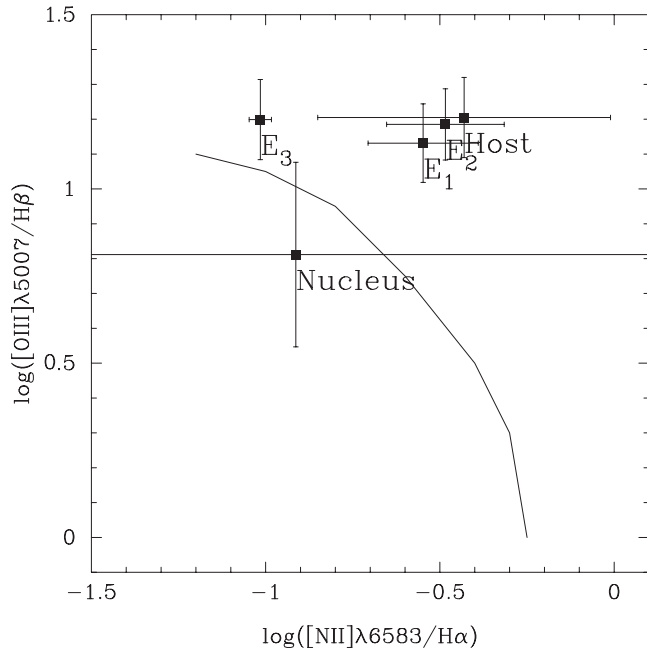


FIG. 10.— $[\text{O III}] \lambda 5007/\text{H}\beta$  vs.  $[\text{N II}] \lambda 6583/\text{H}\alpha$  intensity ratios for the different components of 3C 120. The solid curve divides AGNs from H II region-like objects.

cloud, since a postshock zone can also give rise to the observed line ratios. The similarities between the line ratios for the different EELRs and between them and the host galaxy ones may indicate a similar origin for the ionization, that is, direct photoionization from the UV field of the AGN. In that case the effect of the jet over the  $\text{E}_1$  would be reduced to a split of the cloud and a compression that gives rise to a density enhancement.

#### 5.4. Spectral Energy Distribution of the Continuum-dominated Condensations

Figure 9b shows the spectral energy distribution (SED) of the continuum-dominated structures A, B, and C detected in 3C 120 within the field of view of our IFS data. The SEDs were obtained by an average of the integrated spectra of the different structures extracted from the residual data cube over spectral ranges of 300 Å width. The low intensity of the continuum-dominated structures and the subsequent low signal-to-noise ratio prevent us from using directly the extracted spectra for this analysis. The SEDs were cut at 7500 Å since at larger wavelengths the imperfect subtraction of the skylines and the noise enhancement strongly affect the reliability of the derived SED. Synthetic spectra for three different stellar populations of different ages were included for comparison purposes. These spectra are similar to those shown in Figure 8b (described in § 5.2), but without including the effects of dust. The SEDs are almost flat in the plotted ranges, being roughly consistent with a mix of a young stellar population with an underlying old stellar population. This result agrees with the results based on the broadband colors of the structures, discussed in § 4.2. Therefore, the continuum structures are experiencing a decrease of the dust content, rather than an increase of the star formation. This seems to be particularly valid for the A structure, which lies in a minimum of the dust content, derived from the  $\text{H}\alpha/\text{H}\beta$  line ratio (see Fig. 6e). Unfortunately, we cannot check it for the B and C structures because the gaseous emission in those regions is less luminous and therefore the  $\text{H}\alpha/\text{H}\beta$  ratio is uncertain.

So far only starlight was considered to explain the emission found in the different condensations. However, their SEDs could be also explained considering other components, like scattered light from the nucleus and/or synchrotron emission associated with the radio jet. Hjorth et al. (1995) detected polarization in the condensation A, the direction and magnitude of which were consistent with those found by Walker et al. (1987). This may indicate a connection between that condensation and the radio jet. Indeed, it may indicate that condensation A consists, at least partially, of optical synchrotron emission. However, as was shown in § 4.1 (and noticed by Hjorth et al. 1995), A does not follow the radio jet into the core, being more likely associated with B and C. Furthermore, the measured polarization may be due to unsubtracted scattered light from the nucleus (Hjorth et al. 1995), which we detected in the average spectrum of the host (Fig. 8 and § 5.2). Indeed, the SEDs of the three different condensations do not differ significantly (Fig. 9b), and, in particular, they show almost the same  $V - R$  colors (Fig. 5), which indicates, most probably, a similar origin for all of them. Since most of the scattered light has been removed and the synchrotron radiation could also contaminate A, these condensations are most probably dominated by starlight.

## 6. 3C 120 VELOCITY FIELD

The central wavelengths of the Gaussians fitted to the individual spectra (§ 4.3) give us the radial velocity associated with the ionized gas at each position. Interpolating the individual emission-line centroids, we obtain the velocity field of different emission lines. Uncertainties due to wavelength calibration ( $< 35 \text{ km s}^{-1}$ ) and those related to the fitting process ( $\sim 15 \text{ km s}^{-1}$ ) are small enough to be irrelevant for the following discussion.

Figure 11 shows the velocity field of the ionized gas derived from  $[\text{O III}] \lambda 5007$  and  $\text{H}\alpha$  lines. While  $\text{H}\alpha$  traces the kinematics of low-ionization gas that describes the general pattern of the galaxy,  $[\text{O III}]$  draws the signatures of high-ionization gas, characterizing the most perturbed regions. Previous kinematic studies of 3C 120 found a rather chaotic velocity field (Baldwin et al. 1980) and some slight evidence of a coexisting rotating system (Baldwin et al. 1980; Moles et al. 1988). Despite the different spatial resolution and coverage of the IFS data in this paper, our results are in agreement with those of Baldwin et al. (1980) and Moles et al. (1988) pointing toward highly distorted kinematics in this object.

The unclear morphology and highly distorted gas kinematics of 3C 120 make a simple interpretation of the velocity structure difficult. The ionized gas velocity field presents a general regular pattern, with larger velocities at the northwest and lower at the southeast that may be consistent with a disk rotating around an axis along the northeast direction (Figs. 11a and 11b). Several kinematic perturbations can be identify in the velocity maps, as well as a regular rotation.

A velocity gradient is located  $\sim 5''$  west of the nucleus, aligned with the radio jet (Fig. 3b), at the position of  $\text{E}_1$  (Fig. 11a). Using a better spectral resolution, Axon et al. (1989) show that there are two different kinematic components rather than a velocity gradient. The north component is receding while the south component is approaching. The kinematic perturbation is most probably due to the lateral expansion of the radio jet (Axon et al. 1989): as already quoted, the interaction of the radio jet and the intergalactic gas produces an enhancement of the gas density (§ 4.3) and perturbs the kinematics (Sánchez 2004).

The velocity field derived from  $[\text{O III}]$  is much more distorted to the east (farther than  $4''$  from the nucleus) than that one derived from  $\text{H}\alpha$ . Although the signal-to-noise ratio in the IFS

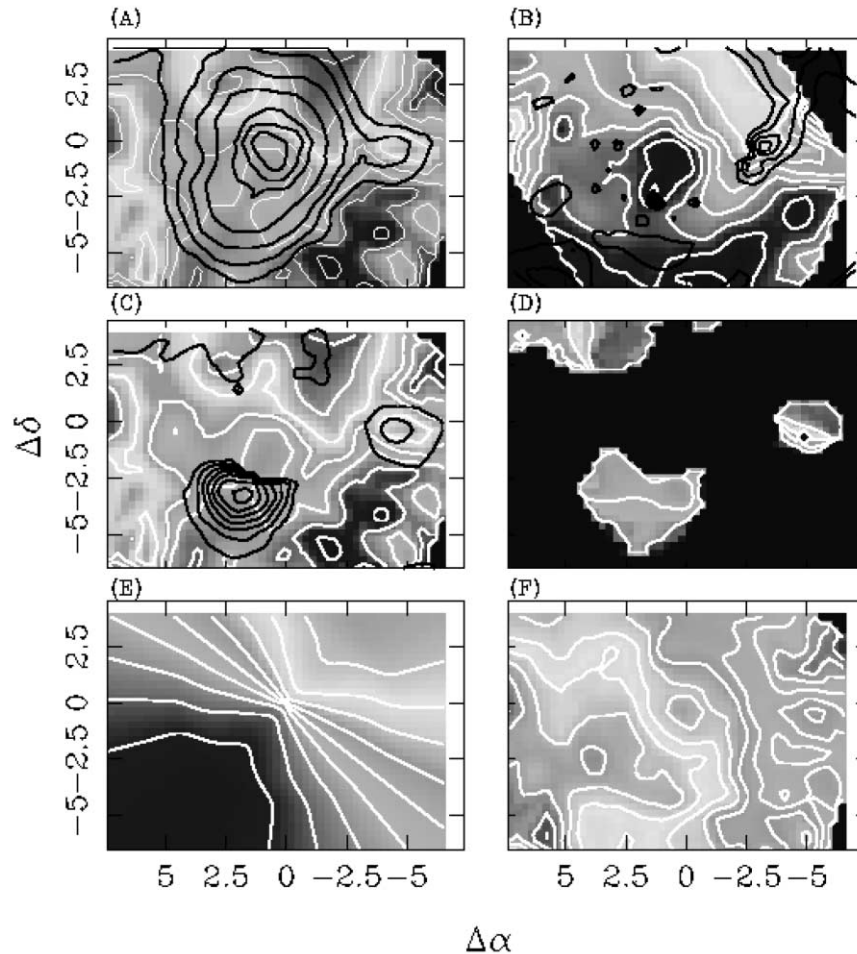


FIG. 11.—Ionized gas velocity fields of 3C 120 derived from the Gaussian fit to (a) [O III], where isovelocity lines extend from 10,200 to 10,600 in steps of  $50 \text{ km s}^{-1}$ ; and (b)  $\text{H}\alpha$ , where isovelocity lines extend from 10,000 to 10,600 in steps of  $50 \text{ km s}^{-1}$ . (c) Same as (a), but with the [O III] intensity of  $E_1$ ,  $E_2$ , and  $E_3$  in black contours. (d) Velocity distribution of ionized gas structures ( $E_1$ ,  $E_2$ ,  $E_3$ ). Isovelocity lines extend from 9600 to 10,300 in steps of  $100 \text{ km s}^{-1}$ . (e) Simplest rotational model obtained considering an inclination of  $40^\circ$  and P.A. =  $-40^\circ$ . (f) Residual velocity map after the subtraction of the rotational model (panel e) from the ionized gas velocity field (panel a). Isovelocity lines correspond to kinematics of structures  $E_1$ ,  $E_2$ , and  $E_3$  as in (d). [See the electronic edition of the Journal for a color version of this figure.]

spectra is low and uncertainties are larger in that region, differences in the kinematics may be explained by the different origin of these lines. The comparison of the continuum-dominated structures and the velocity field derived from the  $\text{H}\alpha$  shows that  $A$  and  $B$  coincide with a velocity distortion located west of the nucleus (Fig. 11b). This kinematic feature is similar to those found in the velocity field of spiral galaxies because of the arms (e.g., Knapen et al. 2004). This gives support to the idea of identifying the  $A$  and  $B$  regions as structures in a spiral arm in 3C 120 in spite of its poor gas content and continuum emission dominated by starlight. We discuss in detail the origin of this armlike structure in § 7.

The comparison of the ionized gas structures  $E_2$  and  $E_3$  (Fig. 7b) and the velocity field gives clues to the origin of the EELRs (Fig. 11c). The morphology of  $E_3$  follows remarkably well an east-west gradient in the velocity map.  $E_2$  is in a close to constant velocity region. Both clouds are in regions that present strong kinematic perturbations from the canonical rotation. These perturbations are more prominent in the velocity structure of the high-ionization gas than that of the low-ionization gas.

Fitting a single Gaussian to the emission lines in the residual data cube of spectra (§ 5), we have derived the velocity behavior of the  $E_1$ ,  $E_2$ , and  $E_3$  residual structures. Figure 11d shows the

velocity map derived from the [O III] lines in the residual spectra. We hereafter refer to this map as the velocity map of residuals. The kinematics of the structures traces remarkably well the perturbations in the velocity field, although their kinematic features are smoother in the latter. The smoothing is a clear consequence of the blending of the host galaxy and the structure spectra. The velocity map of the residuals represents much better the kinematics of the gas clouds in  $E_1$ ,  $E_2$ , and  $E_3$ . We found a clear gradient of velocities in the region corresponding to the three structures pointing to inflows/outflows of gas at different inclination angles and outside of the galactic disk. While regions  $E_1$  and  $E_2$  present a north-south velocity gradient,  $E_3$  shows an east-west gradient in good agreement with the [O III] velocity map (Fig. 11a).

Despite the bulge-dominated morphology found in the inner regions of 3C 120, the velocity field derived from  $\text{H}\alpha$  indicates the presence of a rotating disk along the northwest/southeast (Fig. 11b). In that case, the receding velocities at the northwest suggest that southeast is the face closer to the observer. The velocity gradient also traces the line of zero velocities, but it is not clearly defined in the derived velocity field because of the distortions in the center introduced by the Seyfert 1 nucleus. With a larger spatial coverage, Baldwin et al. (1980) determined

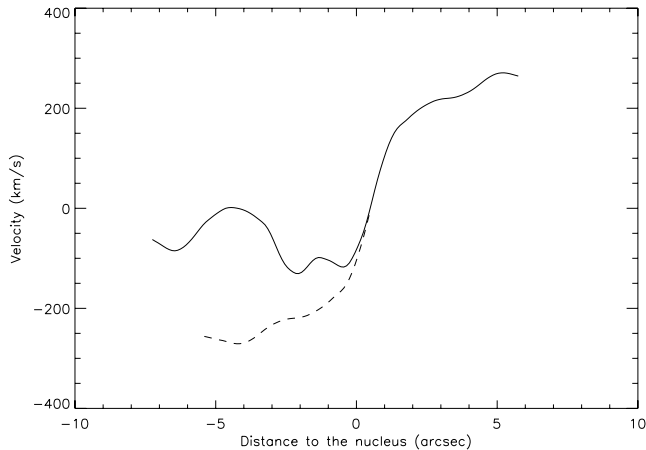


FIG. 12.—*Solid line*:  $H\alpha$  velocity distribution of 3C 120 along a position angle of  $-40^\circ$  from southeast (*left*) to northwest (*right*). The perturbation associated with  $E_2$  is seen as a peak at approximately  $-5''$ . The dashed line shows the distribution obtained assuming that the northwest portion of the velocity distribution describes the behavior of the rotating component of the galaxy and modeling the southeast by a symmetrical distribution.

a P.A. =  $72^\circ \pm 15^\circ$  for the minor kinematic axis. This angle agrees with the semiminor axis determined from the two-dimensional modeling of the galaxy (§ 4.1). A visual inspection of the velocity fields in Figures 11a and 11b indicates that this P.A. may be a good estimation of the minor kinematic axis, when considering the distortion at the west. However, this distortion is most likely produced by the interaction of the radio jet with the  $E_1$  cloud (Sánchez 2004) and most probably is not related to the rotating disk. The isovelocity contours of the velocity field derived from  $H\alpha$  and the position of the kinematic center ( $\sim 0''.8$  northwest of the nucleus) suggest that the minor kinematic axis is most likely along P.A.  $\sim 50^\circ$ , which is not far from the photometric determinations and within their uncertainties. Therefore, we consider hereafter a P.A. =  $-40^\circ$  for the major kinematic axis of 3C 120.

Figure 12 shows the rotation curve of 3C 120 derived from the velocity field of  $H\alpha$ , assuming a P.A. of  $-40^\circ$  for the major kinematic axis. This curve is clearly distorted at the southeast owing to the kinematic perturbations associated with  $E_2$ . However, the northwest portion of the curve is remarkably similar to those of galactic rotating disks (Binney & Merrifield 1998). The effects of the perturbations in the southeast portion of the curve must be removed prior to modeling the two-dimensional distribution of the rotating component of the galaxy. For doing so, it was assumed that the approaching portion of the rotation curve (southeast) follows a symmetrical counterpart of the receding portion (northwest). This *hypothetical* rotation curve was included in Figure 12. This curve was then used to derive a template of the velocity field by applying a simple rotational model (Mihalas & Binney 1981), for different inclinations varying from  $\sim 5^\circ$  to  $\sim 85^\circ$ . Subtracting those templates from the  $H\alpha$  velocity field and minimizing the differences at the northwest region (where the rotation curve really corresponds to the 3C 120 kinematic behavior), we estimated an inclination angle of  $\sim 40^\circ$  for the disk component of 3C 120. The velocity field template corresponding to that inclination angle is shown in Figure 11e. This estimation of the inclination is in agreement with the determination from the external isophote (Moles et al. 1988). As quoted before, the internal isophotes are less elongated and distorted at the west than the external ones. This suggests a different inclination angle, smaller at the inner than at the outer regions.

Indeed, the ellipticities derived from the two-dimensional modeling (§ 4.1) indicate that the inclination may range from  $\sim 20^\circ$  to  $\sim 43^\circ$  in the center, in agreement with the kinematic estimation. The differences in inclination from the center to the outer regions, although small, suggest a slightly warped disk component in 3C 120.

Figure 11f shows the residual of the [O III] velocity map after the subtraction of the rotational model in Figure 11e (hereafter residual velocities). This residual map shows an almost flat area of  $0 \pm 20$  km s $^{-1}$  at the northwest region, within the uncertainties of the velocity determination. At the west, coincident with the path of the radio jet and the location of  $E_1$ , there is a north-south gradient of  $\sim 148$  km s $^{-1}$ , in agreement with the results by Axon et al. (1989). At the location of  $E_2$  there is a rather chaotic residual velocity structure, with velocities ranging from  $\sim 270$  to  $460$  km s $^{-1}$ . A slight east-west gradient of  $\sim 32$  km s $^{-1}$  is found at the location of  $E_3$ . The residual velocities (Fig. 11f) and the velocity map of the residuals (Fig. 11d) present a rather good qualitative agreement in spite of the strong conceptual and practical differences of the two methods used to derive them. This supports the idea of the presence of a rotational component in 3C 120.

Because of the low spectral resolution of our data, no attempt was made to analyze the velocity dispersion maps.

## 7. DISCUSSION

In previous sections we presented several aspects of 3C 120 that describe a puzzling environment. Object 3C 120 is, morphologically speaking, a bulge-dominated galaxy that contains a rotating stellar disk and several continuum-dominated structures and EELRs. We analyzed in detail those structures in order to determine their nature. The  $E_1$  is caused by the interaction of the radio jet with the intergalactic medium, as already discussed in Sánchez et al. (2004a).

The newly reported shells in the central region of 3C 120 are an addition to the complex picture of this object. Shells are common structures in elliptical and S0 galaxies, although a few spirals also show the presence of this kind of feature (Malin & Carter 1983; Schweizer & Seitzer 1988). Although models considering internal shock waves were proposed to account for the presence of shells in galaxies (see, e.g., Williams & Christiansen 1985), the most accepted idea is that they are generated by merging processes (see, e.g., Hernquist & Spergel 1992 and reference therein). Numerical simulations indicate that the number and sharpness of shells in merger remnants depend on the mass ratio and the absence (or presence) of a central bulge in the progenitors (González-García & Balcells 2004). The radial distribution of shells depends on the potential of the host galaxy, and their morphology can appear aligned or randomly distributed around the galaxy (Prieur 1990). Object 3C 120 shows two well-defined shells, labeled  $S_N$  and  $S_S$ , and some other shell-like faint features that are aligned along an axis of P.A.  $\sim -25^\circ$ . When shells are well aligned along a certain axis, this axis is always close to the major axis of the galaxy (Prieur 1990), which is our case. Shells can be found in a wide range of radii from the nucleus, from only a few to hundreds of kiloparsecs, such as in the case of NGC 3923 (Prieur 1988). The innermost shell detected in 3C 120 is at around  $1''$  north ( $\sim 1$  kpc) of the nucleus. Shells found close to the nucleus imply that a dissipative process has played an important role in the formation of the shells (Prieur 1990). Therefore, the presence of the detected circumnuclear shells (§ 4.1) strongly suggests the idea of considering 3C 120 as a late stage merger.

The armlike clumpy structures A and B (§ 4.1) show kinematics that resemble those of a spiral arm as explained in § 6. However, spiral arms are active star-forming regions, and no star formation was detected in either of the continuum-dominated structures. In that case, these structures could be also the remnant of a merging process. Indeed, the regions B, A, and  $S_5$  seem to be connected in our residual and color maps (Figs. 3c and 4b), and  $S_5$  is associated with the  $E_2$  EELR. A kinematic feature (Fig. 11b) is coincident with these structures. Numerical simulations indicate that these kinds of structures are found as remnants of merging processes (e.g., Howard et al. 1993; Heyl et al. 1996; Mihos & Hernquist 1996) and are difficult to explain by any other mechanism. Assuming that scenario, the presence of an overdensity of gas in the south shell may indicate an inflow, where the warmer gas has dropped faster into the inner regions. This picture is in good agreement with the kinematic features at the south shell ( $E_2$  cloud kinematics) and its residuals. The regular velocity in this region suggests that this inflow may occur in a plane outside the galactic disk and close to the line of sight. Although the kinematics of the merger remnants strongly depends on the viewpoint, the velocity and velocity dispersion measured for  $E_2$  are in good agreement with merger simulations (Heyl et al. 1996). Theoretical models indicate that inflows channeling gas from the outer to the nuclear regions may appear in the late stages of a merging process (e.g., Mihos & Hernquist 1996). These inflows have been already observed in different merging galaxies (e.g., Arribas & Colina 2002, 2003). The discussion above suggests that the structures A, B, and  $E_2$  can be identified with a tidal tail driving material to the central region, most probably as a result of a past merger event in 3C 120. Most of the analyzed continuum-dominated structures show a rather young stellar population, indicating a recent (but not ongoing) star formation rate. This result agrees with the picture of a postmerging event. Similar results have been found in the study of the optical colors of host galaxy AGNs (Jahnke et al. 2004a; Sánchez et al. 2004b).

The poor spatial coverage of the third identified EELR,  $E_3$ , prevents us from drawing a clear picture of its origin. In fact, this region corresponds (see § 5.1) to a tail extension of a larger structure already reported in this object (Soubeyran et al. 1989). Although we cannot be conclusive with our current data, the kinematic results most probably indicate that  $E_3$  is associated with an inflow/outflow of gas to/from the circumnuclear region.

It has long been suggested that strong interactions and galaxy mergings may (re)ignite nuclear activity (e.g., Sanders et al. 1988). Galaxy interactions can produce the loss of momentum required to allow the infall of gas toward the nuclear regions, gas that would feed the AGN. Many authors found that AGN hosts show distorted morphologies, reminiscent of past merging events (e.g., McLeod & Rieke 1994a, 1994b; Bahcall et al. 1997; Sánchez & González-Serrano 2003). They are found in environments with high probability of experiencing interactions (e.g., Sánchez & González-Serrano 2002), and their hosts, mostly early-type galaxies, present anomalous blue colors (e.g., Sánchez et al. 2004a). All together it may indicate that, if not all, at least a family of AGNs is generated by the merging/interaction between galaxies (Canalizo & Stockton 2001). A merging event alone is not enough to generate an AGN. The presence of a massive black hole in the progenitor galaxy is a basic requirement. Massive black holes are only found in bulge-dominated massive galaxies, as a result of the black hole/bulge mass relation (e.g., Magorrian et al. 1998; Kormendy & Gebhardt 2001). Indeed, recent results (S. F. Sánchez et al. 2005, in prep-

aration) show that the fraction of AGNs increases in galaxy mergers between two large galaxies or between a large and a small galaxy.

Our current results agree with this scenario. Object 3C 120 is a bulge-dominated galaxy that has, most probably, experienced a merging event with a less massive galaxy. That galaxy was completely disrupted in the merging process, falling in parts that produce, most probably, many of the observed structures (Moles et al. 1988). This may explain the different stellar populations of the structures and the average stellar population in the object (§ 4.2) as has been previously reported for other galaxies (Prieur 1990). A substantial fraction of its gas has been channeled toward the inner regions, following the detected armlike structure, and concentrating in the  $E_2$  region.

## 8. SUMMARY

We obtained integral field optical spectroscopy of the Seyfert 1 radio galaxy 3C 120. The homogeneous data, excellent spatial and spectral coverage, and good spatial and spectral resolution make this atlas a useful tool for studying 3C 120 in the optical. These IFS optical data were combined with high-resolution *HST* imaging. The analysis of these data suggests that a Seyfert 1 nucleus at the center, an early-type galaxy, and several structures that formed as a consequence of a merging process in the past constitute the radio galaxy 3C 120. At least one of these structures is identified with an inflow, which is feeding the central engine. A radio jet is escaping from the center, perturbing the gas on its path.

The main results from the analysis of this data set were as follows:

1. Several continuum-dominated structures were detected in 3C 120, which do not follow the mean distribution (bulge dominated) of the stellar component. Some of these structures were shells in the central kiloparsec of the object, which may indicate a past merging process. The colors of the different components were not compatible with a single stellar population in this galaxy.
2. Three emission-line structures were identified ( $E_1$ ,  $E_2$ , and  $E_3$ ) that were not associated with the general behavior of the galaxy. These gaseous structures presented a high level of ionization. The origin of structure  $E_1$  was the interaction between the intergalactic medium and the radio jet emerging from the nucleus.
3. The spectra of the nucleus and the host galaxy were decoupled, obtaining a data cube of residuals. From that residual data cube, we extracted and analyzed the spectra of the different structures in 3C 120.
4. The velocity field indicated a rotational component plus several kinematic perturbations associated with the identified emission structures.
5. The continuum-dominated structures A, B, the  $S_5$  shell, and the EELR  $E_2$  seem to be physically associated, belonging to the innermost part of a tidal tail, a remnant of a past merging event. This tail has channeled gas into the inner regions, in an inflow, that has generated  $E_2$ .

The 4.2 m William Herschel Telescope is operated by the Isaac Newton Group at the Observatorio de Roque de los Muchachos of the Instituto de Astrofísica de Canarias. We thank all the staff at the Observatory for their kind support. This

project is part of the Euro3D RTN on IFS, funded by the EC under contract HPRN-CT-2002-00305. This project has used images obtained from the *HST* archive, using the ESO archiving facilities. We would like to thank R. C. Walker for kindly pro-

viding us with the radio maps of 3C 120. We would like to thank C. González-García for his useful comments. We would like to thank the anonymous referee, who has helped up to improve the quality of this paper with his/her remarks.

## APPENDIX A

### ATLAS OF SPECTRA

In this appendix we present the spatial distribution of the brightest emission-line profiles as spectral diagrams. These diagrams represent line profiles in a short wavelength range of the individual spectra at each point (fiber). The spectra at each location are autoscaled to show the profile shape (lines nearer to the optical nucleus are brighter than those farther out). Figures 13 and 14 show the spectral diagrams corresponding to  $H\beta + [O\text{ III}] \lambda\lambda 4959, 5007$  and  $H\alpha + [N\text{ II}] \lambda\lambda 6548, 6584 + [S\text{ II}] \lambda\lambda 6716, 6730$ , respectively. A considerable blending of the emission lines with the wings of the broad component of the Balmer lines can be clearly appreciated in these diagrams.

## APPENDIX B

### DECOUPLING THE SPECTRA OF DIFFERENT COMPONENTS USING IFS

A new technique to decouple the spectra of different components in an object has been developed, based on well-known techniques applied in the decoupling of different components in images. Two different methods have been developed. The first one is based on a two-dimensional modeling of the objects using object templates, while the second one is based on an isophotal analysis of two-dimensional images. We explain here how both methods have been extended to the analysis of IFS data cubes, as well as the advantages of each one.

#### B1. THREE-DIMENSIONAL MODELING

IFS combines the characteristics of imaging and spectroscopy. In general terms, IFS data consist of a series of spectra obtained at a discrete number of positions in the sky. In the case of INTEGRAL data in the SB2 configuration, they consist of the 209 spectra obtained in the same number of positions in the sky. Newer instruments, like PMAS (Roth et al. 2000) or VIMOS (LeFevre et al. 2003), sample the sky in a continuous way, by coupling the fibers to lens arrays. In the latter cases an IFS data cube can be understood

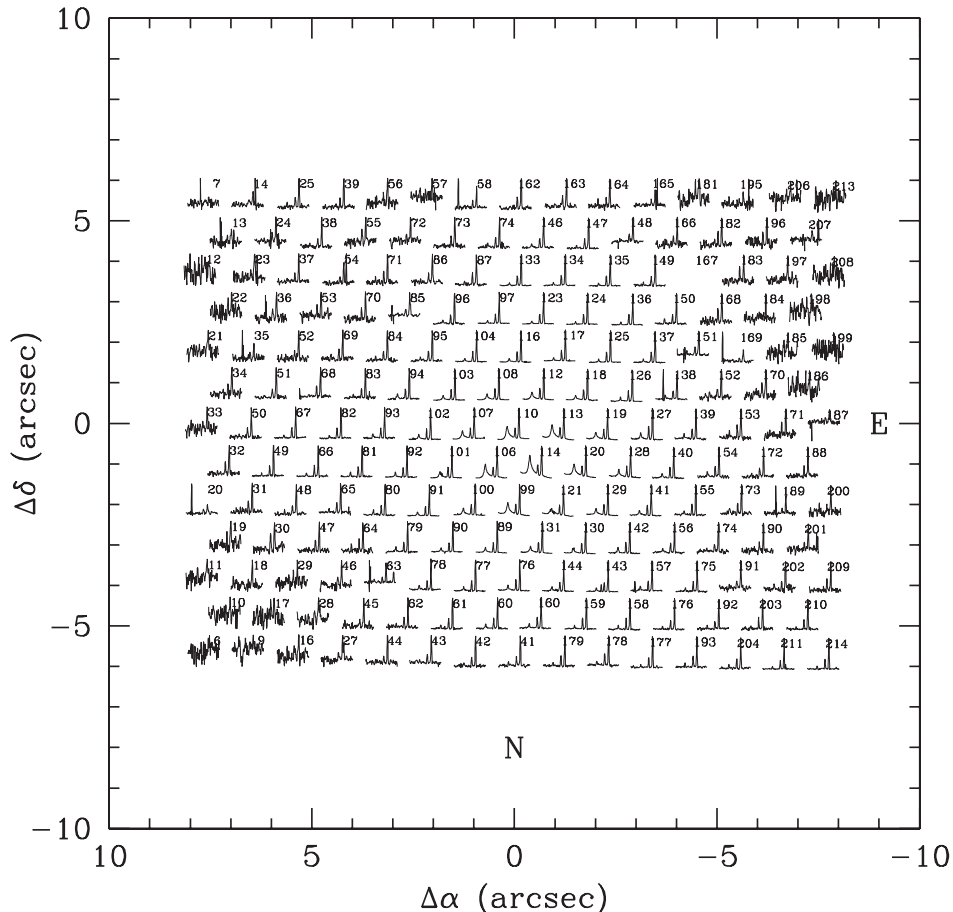


FIG. 13.—Two-dimensional spectroscopic diagram of  $H\beta + [O\text{ III}] \lambda\lambda 4959, 5007$  emission line profiles. Plotted spectral range: 4910–5300 Å.

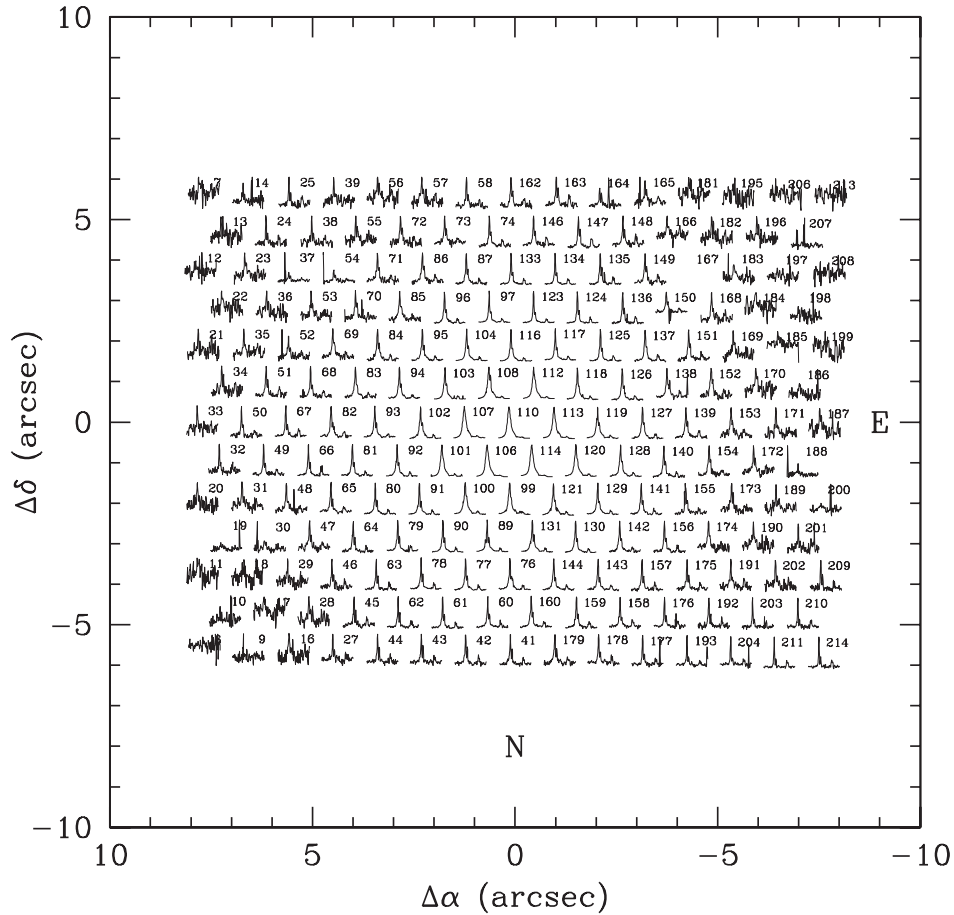


FIG. 14.—Two-dimensional distribution of emission-line profiles of  $H\alpha + [N \text{ II}] \lambda\lambda 6548, 6584 + [S \text{ II}] \lambda\lambda 6716, 6730$ . The spectral range plotted is 6650–7050 Å.

as a stack of narrowband images. More generally, at each wavelength we have a two-dimensional discrete distribution of fluxes, which can be transformed to a regular grid distribution by an interpolation routine.

It is a quite common situation that an observed object is the combination of different components, e.g., a QSO lens, a crowded field of stars, and an AGN+host system. Different techniques have been developed to decouple the different components of an image and to derive their photometry. A wide extended technique is to fit the images with a two-dimensional model, including a template for each different component. This technique is implemented in GALFIT (Peng et al. 2002), a program for modeling multiple components in images. This program has been used in the decoupling of nuclear and host components (Sánchez et al. 2004b) and the decoupling of different components in a QSO lens (Wisotzki et al. 2004). GALFIT fits the images with a multicomponent model, producing a template image and a residual image. This residual image can be used to detect substructures in two-dimensional images.

A natural extension of the two-dimensional modeling technique to IFS is to split the data cube into a set of narrowband images of the width of the spectral pixel (the so-called monochromatic images) and treat them as individual images. This technique has been used successfully for the deblending of QSO lenses with IFS (Wisotzki et al. 2003). In the particular case of our INTEGRAL data, we first transformed the discrete set of spectra in a regular grid data cube using an interpolation routine implemented in E3D (Sánchez 2004). The final data cube has a  $0''.3 \times 0''.3$  pixel size, i.e.,  $\frac{1}{3}$  of the original diameter of the fibers.

The two-dimensional image modeling of the nucleus and the host for each monochromatic image was performed using GALFIT. The two-dimensional model comprises a narrow Gaussian function (to model the nucleus) and a de Vaucouleurs law (to model the galaxy), both convolved with a PSF. The PSF at each wavelength was obtained from a calibration star data cube, observed just before the object. In a first attempt all the parameters of the model were fitted: the intensities of the nucleus and the host, the centroid of the object, the effective radius, the position angle, and the ellipticity of the host galaxy. As already noticed by Wisotzki et al. (2003), this first modeling does not produce acceptable results. The large number of parameters, the degeneracy between some of them (e.g., the total intensity and the scale length), and the limited sampling of our data impose limitations to the quality of the recovered spectra.

However, Wisotzki et al. (2003) demonstrated that it is possible to increase the quality of the modeling by imposing certain conditions in the structural parameters. The centroid of the object varies through the wavelengths as a result of differential atmospheric refraction (DAR; Filippenko 1982). Therefore, whenever there is a clear peak in the object (like in our case), the centroid should vary smoothly with the wavelength. Figure 15 shows the centroid coordinates as a function of the wavelength resulting from the three-dimensional modeling. Despite the fluctuations, there is a clear trend. The solid lines show the result of fitting a polynomial function of order 5. In a second run of the three-dimensional modeling we imposed the centroid to be fixed to the result from this polynomial fitting. Similar conditions can be imposed for the ellipticity, effective radius, and position angle of the host galaxy. By forcing the structural parameters to vary smoothly with the wavelength and fixing them in the three-dimensional modeling process,

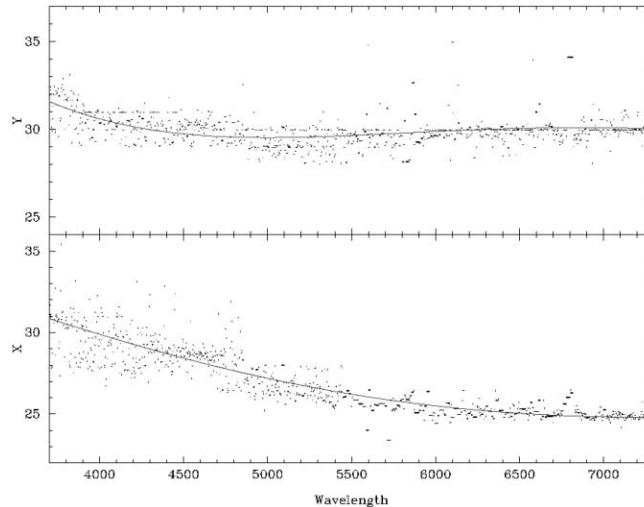


FIG. 15.—Centroid coordinates,  $x$  and  $y$ , in pixels ( $0''.3 \text{ pixel}^{-1}$ ), as a function of the wavelength as derived from the first run of the three-dimensional modeling. The solid lines show the result of the fitting with a polynomial function. [See the electronic edition of the Journal for a color version of this figure.]

the number of parameters is reduced to the intensity of the different components. Thus, the accuracy of the modeling is increased (Wisotzki et al. 2003, 2004).

The number of parameters can be reduced too if we derive the structural parameters from an external source of information. As we explained above, we have good-quality *HST* images of the object in different bands, which have already been analyzed using GALFIT (§ 4.1). We fixed the structural parameters (effective radius, ellipticity, and position angle) in our second three-dimensional modeling of the values derived by the two-dimensional modeling of the *HST* images (Table 2). The centroids were fixed to the values derived using the polynomial function shown in Figure 15. Figure 16 illustrates the process. The top left panel shows the decoupled spectra of the nucleus and the host derived from the three-dimensional modeling when all the parameters are fitted freely. The spectra derived from the first run are noisy and can only be considered a very rough approximation. The top right panel shows the spectra derived from the modeling when the centroid is fixed to the result of the polynomial function fitting shown in Figure 15. There is a clear increase of the quality of the derived spectra. The bottom left panel shows the spectra when, in addition to the centroids, the structural parameters of the host galaxy (ellipticity, position angle, and effective radius) are fixed to the result from a polynomial function fitting similar to the one used for the centroids. This is the best possible result if we only had the information from the IFS. The bottom right panel shows the final result, obtained when the structural parameters are fixed to the values derived from the two-dimensional modeling of the *HST* images. The derived spectra are remarkably similar to those of the previous case. However, in the previous case it is possible to identify some *fake* absorption features in the spectrum of the nucleus coincident with the narrow emission lines (e.g., [O III]  $\lambda 5007$ ). We cross-checked the accuracy of the final decoupled spectra by comparing the fluxes derived with those obtained by the two-dimensional modeling of the *HST* images. Both fluxes agree within  $\sim 20\%$ .

As we explained above, GALFIT provides us with a residual image at each wavelength after the subtraction of the two-dimensional model from each monochromatic image. We stored and stacked those residual images to create a residual data cube. The residual data cube is used (1) to cross-check the accuracy of the fitting (i.e., no evident fake residuals are found) and (2) to study the substructures in the object. The left panel of Figure 17 shows a narrowband image centered in the continuum adjacent to the [O III] emission line ( $5204\text{--}5246 \text{ \AA}$ ) from the residual data cube (*contour plots*), together with the residual image obtained by a two-dimensional modeling of the *HST* F555W-band image (*gray scale*). A simple comparison of both images shows that the residuals are remarkably similar outside  $\sim 2''$  from the nucleus. However, there is a ring structure at  $\sim 1''.5$ ,  $\sim 100$  times fainter than the nucleus, especially bright in the  $S_S$  of the nucleus. This structure coincides somehow with the southeast shell. However, it is worrisome that it is fainter in the northwest, where the  $S_N$  shell is brighter. Taking into account the original size of the fibers ( $\sim 0''.9$ ) and our limited determination of the PSF, we think that this ring substructure is an artifact of the two-dimensional modeling. Although it limits the use of the residual data cube to study the properties of the substructures, it does not significantly affect the accuracy of the decoupled spectra.

## B2. THREE-DIMENSIONAL SURFACE BRIGHTNESS ANALYSIS

We developed a second method to create a three-dimensional template of the object that would not depend on the PSF determination and without assuming any certain law to describe the intensity profile. This method is an extension of the isophotal surface brightness analysis technique (Jedrzejewski 1987). It looks for the ellipse parameters that better represent the isophotal shape by a Fourier analysis of the surface brightness at a certain radius as a function of the eccentric anomaly. The output is a surface brightness profile of the object (i.e., the radial distribution of the intensity) and the radial distributions of the centroid, position angle, and ellipticity (understanding radius as semimajor axis of the ellipse). A template of the object is created using these output parameters. Then, a residual of the image is obtained by subtracting this template from the original image. This technique has been extensively used for the detection of substructures in galaxies for decades (e.g., Pérez-Fournon et al. 1986; Hjorth et al. 1995).

We extended this method to analyze substructures in IFS data. For each monochromatic image we performed an isophotal surface brightness analysis using our own coded routines. The average centroids, ellipticities, position angles, and the integrated fluxes

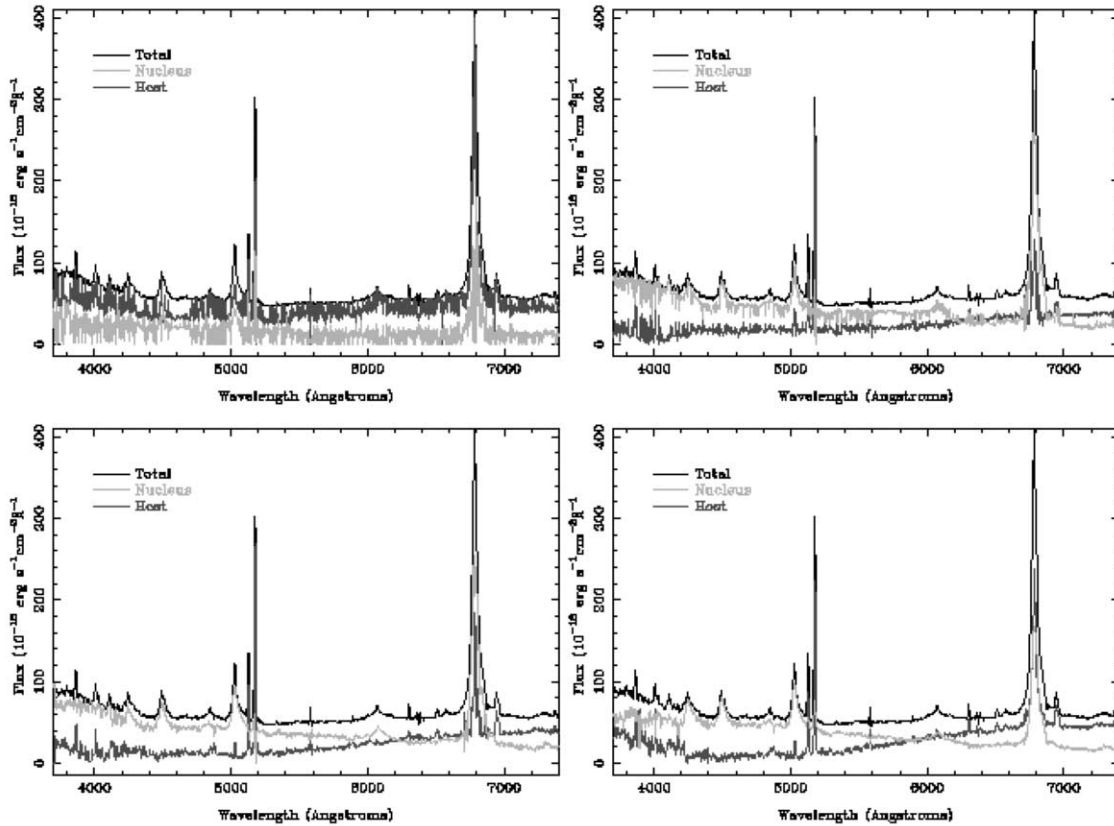


FIG. 16.—*Top left*: Decoupled spectra of the nucleus and the host of 3C 120, together with the total spectrum of the object, derived from the three-dimensional modeling when all the parameters are fitted freely. *Top right*: Similar spectra derived from the modeling when the centroid is fixed to the result of the polynomial function fitting shown in Fig. 15. *Bottom left*: Similar spectra derived when, in addition to the centroids, the ellipticity, position angle, and effective radius of the host galaxy are fixed to the result of a polynomial function fitting as a function of the wavelength. *Bottom right*: Final decoupled spectra obtained when the structural parameters of the host galaxy are fixed to the values derived from the two-dimensional modeling of the *HST* images. [See the electronic edition of the *Journal* for a color version of this figure.]

obtained from this analysis are stored for each wavelength. The residual images obtained are combined in a residual data cube. As in the previous method, the quality of the model template can be increased assuming that the structural parameters change smoothly with the wavelength. The structural parameters for each wavelength were fixed to the values derived by a polynomial function fitting. In the case of an isophotal analysis, after the structural parameters were fixed, the derived model for each monochromatic image is just estimated by obtaining the average flux at a certain radius along the eccentric anomaly. In other words, it is not a fit anymore, but just a direct measurement.

Figure 18 illustrates the results of this process. It shows, in both panels, the integrated spectrum of 3C 120 over the field of view of INTEGRAL (*black line*), together with the recovered spectrum from the three-dimensional template (*gray line*), and the integrated spectrum of the residuals. The left panel shows the result from the first iteration where all the structural parameters are derived by the described method. In general terms the spectrum of the model matches well the original spectrum, despite some wavelengths where

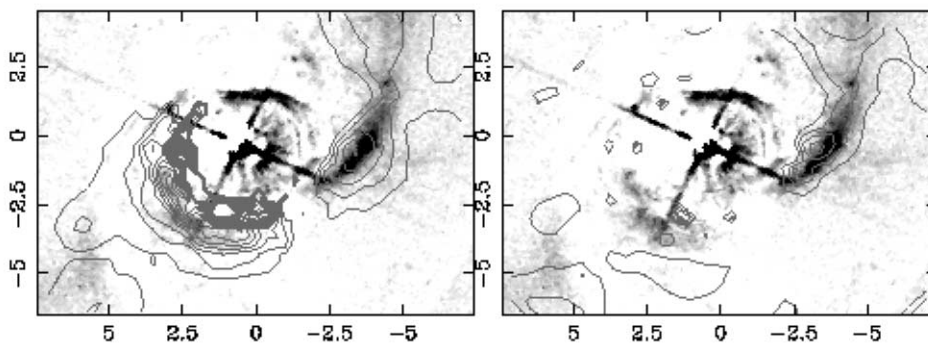


FIG. 17.—*Left*: Contour plot of a narrowband image centered on the continuum adjacent to the [O III] emission line (5204–5246 Å) from the residual data cube obtained by the three-dimensional modeling. *Right*: Contour plot of a narrowband image centered on the continuum adjacent to the [O III] emission line (5204–5246 Å) from the residual data cube obtained by the three-dimensional surface brightness analysis. In both panels the gray scale shows the residual from the two-dimensional modeling of the F555W-band image (Fig. 3d). [See the electronic edition of the *Journal* for a color version of this figure.]

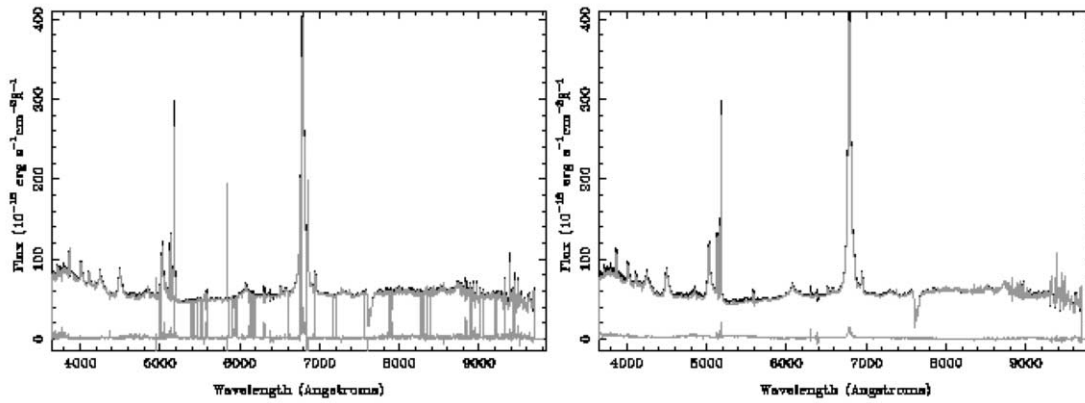


FIG. 18.—*Left*: Integrated spectrum of 3C 120 (black line), together with the spectrum of the model and the residuals, obtained using the three-dimensional surface brightness analysis. *Right*: Similar spectra as in the left panel, obtained once the structural parameters are fixed to the result of a polynomial function fitting as a function of the wavelength. [See the electronic edition of the Journal for a color version of this figure.]

the program is unable to derive the correct parameters. The right panel shows the result from the second iteration with all the structural parameters fixed, as described above. In this case the agreement between the recovered and the original spectrum is remarkably good, with no flux deviation higher than a few percent at any wavelength.

As expected, this method produces a better quality residual data cube than the three-dimensional modeling. The basic reason is that we reduced the number of assumptions about the shape of the object and transformed a fit to a direct measurement. The right panel of Figure 17 shows a similar narrowband image of the continuum adjacent to [O III] from the residual data cube to the one presented in the left panel, but obtained with the three-dimensional surface brightness analysis. The gray scale shows once more the residual from the two-dimensional modeling of the F555W-band image. The residuals from the narrowband image and the *HST* data match better than those of the two-dimensional modeling. No trace of the ring structure is present, which reinforces our idea that it is a spurious result due to a limited sampling and inaccuracies in the PSF determination.

The two developed techniques for decoupling spectra of different components from IFS data give successful results. The first method could be useful for deblending spectra, such as in the case of spectra from different components. The second procedure is more suitable to study the residual structures once the spectrum of the main component is subtracted.

#### REFERENCES

- Arribas, S., & Colina, L. 2002, *ApJ*, 573, 576  
 ———. 2003, *ApJ*, 591, 791  
 Arribas, S., Mediavilla, E., García-Lorenzo, B., del Burgo, C., & Fuensalida, J. J. 1999, *A&AS*, 136, 189  
 Arribas, S., et al. 1998, *Proc. SPIE*, 3355, 821  
 Axon, D. J., Pedlar, A., Unger, S. W., Meurs, E. J. A., & Whittle, D. M. 1989, *Nature*, 341, 631  
 Bahcall, J. N., Kirhakos, S., Saxe, D. H., & Schneider, D. P. 1997, *ApJ*, 479, 642  
 Baldwin, J. A., Carswell, R. F., Wampler, E. J., Boksenberg, A., Smith, H. E., & Burbidge, E. M. 1980, *ApJ*, 236, 388  
 Bingham, R. G., Gellatly, D. W., Jenkins, C. R., & Worswick, S. P. 1994, *Proc. SPIE*, 2198, 56  
 Binney, J., & Merrifield, M. 1998, *Galactic Astronomy* (Princeton: Princeton Univ. Press)  
 Bruzual, G., & Charlot, S. 2003, *MNRAS*, 344, 1000  
 Cairós, L. M., Caon, N., García-Lorenzo, B., Vílchez, J. M., & Muñoz-Tuñón, C. 2002, *ApJ*, 577, 164  
 Canalizo, G., & Stockton, A. 2001, *ApJ*, 555, 719  
 Chabrier, G. 2003, *PASP*, 115, 763  
 de Vaucouleurs, G. 1948, *Ann. d'Astrophys.*, 11, 247  
 Filippenko, A. V. 1982, *PASP*, 94, 715  
 Fitzpatrick, E. L. 1999, *PASP*, 111, 63  
 Fraix-Burnet, D., Golombek, D., & Macchetto, F. D. 1991, *AJ*, 102, 562  
 Fukugita, M., Shimasaku, K., & Ichikawa, T. 1995, *PASP*, 107, 945  
 García-Lorenzo, B., Acosta-Pulido, J. A., & Megias-Fernández, E. 2002, in *ASP Conf. Ser. 282, Galaxies: The Third Dimension*, ed. M. Rosado, L. Binette, & L. Arias (San Francisco: ASP), 501  
 García-Lorenzo, B., Arribas, S., & Mediavilla, E. 2001, *A&A*, 378, 787  
 González-García, C., & Balcells, M. 2004, *MNRAS*, submitted (astro-ph/0411645)  
 Hansen, L., Jorgensen, H. E., & Norgaard-Nielsen, H. U. 1987, *A&AS*, 71, 465  
 Hernquist, L., & Spiegel, D. N. 1992, *ApJ*, 399, L117  
 Heyl, J. S., Hernquist, L., & Spiegel, D. N. 1996, *ApJ*, 463, 69  
 Hjorth, J., Vestergaard, M., Sorensen, A. N., & Grundahl, F. 1995, *ApJ*, 452, L17  
 Howard, S., Keel, W. C., Byrd, G., & Burkey, J. 1993, *ApJ*, 417, 502  
 Hua, C. T. 1988, *A&A*, 199, 105  
 Jahnke, K. 2002, Ph.D. thesis, Univ. Hamburg  
 Jahnke, K., Kuhlbrodt, B., & Wisotzki, L. 2004a, *MNRAS*, 352, 399  
 Jahnke, K., Wisotzki, L., Sánchez, S., Christensen, L., Becker, T., Kelz, A., & Roth, M. 2004b, *Astron. Nachr.*, 325, 128  
 Jedrzejewski, R. I. 1987, *MNRAS*, 226, 747  
 Knapen, J. H., Whyte, L. F., de Blok, W. J. G., & van der Hulst, J. M. 2004, *A&A*, 423, 481  
 Kormendy, J., & Gebhardt, K. 2001, in *AIP Conf. Proc. 586, 20th Texas Symposium on Relativistic Astrophysics*, ed. J. C. Wheeler & H. Martel (New York: AIP), 363  
 LeFevre, O., et al. 2003, *Proc. SPIE*, 4841, 1670  
 Lilly, S. J., & Longair, M. S. 1984, *MNRAS*, 211, 833  
 Magorrian, J., et al. 1998, *AJ*, 115, 2285  
 Malin, D. F., & Carter, D. 1983, *ApJ*, 274, 534  
 McCarthy, P. J., van Breugel, W., Spinrad, H., & Djorgovski, S. 1987, *ApJ*, 321, L29  
 McLeod, K. K., & Rieke, G. H. 1994a, *ApJ*, 420, 58  
 ———. 1994b, *ApJ*, 431, 137  
 Mediavilla, E., et al. 1998, *ApJ*, 503, L27  
 Mihalas, D., & Binney, J. 1981, *Galactic Astronomy: Structure and Kinematics* (2nd ed.; San Francisco: Freeman)  
 Mihos, J. C., & Hernquist, L. 1996, *ApJ*, 464, 641  
 Moles, M., del Olmo, A., Masegosa, J., & Perea, J. D. 1988, *A&A*, 197, 1  
 Motta, V., et al. 2002, *ApJ*, 574, 719  
 Ogle, P. M., Davis, S. W., Antonucci, R. R. J., Colbert, J. W., Malkan, M. A., Page, M. J., Sasseen, T. P., & Tornikoski, M. T. 2005, *ApJ*, 618, 1390  
 Osterbrock, D. E. 1989, *Astrophysics of Gaseous Nebulae and Active Galactic Nuclei* (Mill Valley: University Science Books)  
 Peng, C. Y., Ho, L. C., Impey, C. D., & Rix, H. 2002, *AJ*, 124, 266  
 Pérez-Fourmon, I., Colina, L., Biermann, P., & Marcaide, J. M. 1986, in *IAU Symp. 119, Quasars*, ed. G. Swarup & V. K. Kapahi (Dordrecht: Kluwer), 127  
 Phillips, M. M., & Osterbrock, D. E. 1975, *PASP*, 87, 949  
 Prieur, J. L. 1988, *ApJ*, 326, 596  
 ———. 1990, in *Dynamics and Interactions of Galaxies*, ed. R. Wielen (Berlin: Springer), 72

- Readhead, A. C. S., Pearson, T. J., Cohen, M. H., Ewing, M. S., & Moffet, A. T. 1979, *ApJ*, 231, 299
- Roth, M. M., et al. 2000, *Proc. SPIE*, 4008, 277
- Sánchez, S. 2004, *Astron. Nachr.*, 325, 167
- Sánchez, S. F., García-Lorenzo, B., Mediavilla, E., González-Serrano, J., & Christensen, L. 2004a, *ApJ*, 615, 156
- Sánchez, S. F., & González-Serrano, J. I. 2002, *A&A*, 396, 773
- . 2003, *A&A*, 406, 435
- Sánchez, S. F., et al. 2004b, *ApJ*, 614, 586
- Sanders, D. B., Soifer, B. T., Elias, J. H., Neugebauer, G., & Matthews, K. 1988, *ApJ*, 328, L35
- Sargent, W. L. W. 1967, *PASP*, 79, 369
- Schweizer, F., & Seitzer, P. 1988, *ApJ*, 328, 88
- Sèrsic, J. L. 1968, in *Atlas de Galaxes Australes* (Cordoba: Obs. Astron.)
- Soubeyran, A., Wlerick, G., Bijaoui, A., Lelievre, G., Bouchet, P., Horville, D., Renard, L., & Servan, B. 1989, *A&A*, 222, 27
- Stone, R. P. S. 1977, *ApJ*, 218, 767
- Tadhunter, C. N., Dickson, R. C., & Shaw, M. A. 1996, *MNRAS*, 281, 591
- Tody, D. 1986, *Proc. SPIE*, 627, 733
- Veilleux, S., & Osterbrock, D. E. 1987, *ApJS*, 63, 295
- Walker, R. C. 1997, *ApJ*, 488, 675
- Walker, R. C., Benson, J. M., & Unwin, S. C. 1987, *ApJ*, 316, 546
- Walker, R. C., Walker, M. A., & Benson, J. M. 1988, *ApJ*, 335, 668
- Williams, R. E., & Christiansen, W. A. 1985, *ApJ*, 291, 80
- Wisotzki, L., Becker, T., Christensen, L., Helms, A., Jahnke, K., Kelz, A., Roth, M. M., & Sánchez, S. F. 2003, *A&A*, 408, 455
- Wisotzki, L., Schechter, P. L., Chen, H.-W., Richstone, D., Jahnke, K., Sánchez, S. F., & Reimers, D. 2004, *A&A*, 419, L31
- Zirbel, E. L., & Baum, S. A. 1998, *ApJS*, 114, 177
- Zwicky, F., & Zwicky, M. A. 1971, *Catalogue of Selected Compact Galaxies and of Post-Eruptive Galaxies* (Zurich: Offsetdruck Speich)